N_2O Decomposition Reaction over Cu modified ZSM-5, SAPO-34 and SAPO-41 Zeolite Catalysts: Effects of Oxygen Concentration and Hydrothermal Stability

Thesis for M. Sc. in Sustainable Chemical and Process Engineering

By

Ghazal Askari

Student ID- 2302627

Supervisor:

Dmitry Yu. Murzin

Laboratory of Industrial Chemistry and Reaction Engineering

Johan Gadolin Process Chemistry Centre

Faculty of Science and Engineering / Chemical Engineering

Åbo Akademi University

Turku / Åbo

Acknowledgements

The research presented in this thesis was conducted at the Laboratory of Industrial Chemistry and Reaction Engineering, Johan Gadolin Process Chemistry Centre, Department of Chemical Engineering at Åbo Akademi University, from June to December 2025.

I gratefully acknowledge the financial support provided by the Business Finland projects Casemate (3389/31/2022) and Flex-CPT (7166/31/2023), which made this research possible.

I wish to express my profound and sincere gratitude to my supervisors, Professor Dmitry Yu. Murzin, Docent Narendra Kumar, Dr. Kari Eränen, and Dr. Jari Böling, whose guidance, dedication, and unwavering support were instrumental throughout the course of this research.

I am deeply honored to express my utmost respect and gratitude to **Professor Dmitry Yu. Murzin**, whose exceptional scientific leadership, integrity, and vision shaped every stage of this work. I am sincerely thankful for the opportunity to work under his supervision in his internationally recognized laboratory and for the trust he placed in me by assigning this important research project. His rigorous scientific standards, insightful guidance, and constant encouragement were fundamental to the successful completion of this thesis and have left a lasting impact on my way of thinking as a researcher.

I would also like to express my deepest appreciation to **Docent Narendra Kumar**, whose profound knowledge, dedication to teaching, and generosity in sharing expertise in catalyst synthesis and characterization greatly enriched this research. His patient mentorship, thoughtful discussions, and continuous guidance significantly strengthened my scientific understanding and made this work both rigorous and rewarding.

I sincerely thank **Dr. Kari Eränen**, laboratory engineer, for his outstanding technical expertise and constant theoretical support, which greatly facilitated the progress of my experimental work. I am also grateful to **Dr. Jari Böling** for his leadership based on trust and openness. His encouragement of independent thinking and respect for new ideas played a crucial role in shaping the direction and development of this research.

I gratefully acknowledge **Docent Atte Aho** for his continuous support, insightful discussions on data analysis, and training in advanced characterization techniques, which provided a strong foundation for my scientific development.

I would like to sincerely thank **Linus Silvander** for providing SEM data, and **Ilari Angervo** for his valuable support with XRD analysis. Their expertise and contributions were essential to this study.

My heartfelt appreciation goes to **Dr. Luis A. Gallego-Villada** for his valuable scientific insights and guidance and to PhD student **Olha Yevdokimova** for her assistance with TEM imaging, which added significant depth and quality to this research. I am truly grateful for their kindness and support.

I also wish to thank all my colleagues in the laboratory, as well as my **friends** in Finland and Iran, for creating a welcoming, supportive, and intellectually stimulating environment. To my classmates and friends, thank you for your encouragement, friendship, and shared experiences, which made my master's journey both meaningful and unforgettable.

Above all, I owe my deepest gratitude to my family, whose love, sacrifices, and unwavering support made this journey possible. My **mother** has been the true foundation of my life and education. Her endless patience, strength, prayers, and unconditional love have guided me through every challenge and moment of uncertainty. Her belief in me never wavered, even when the path was difficult, and her sacrifices made it possible for me to pursue my education and dreams. No words can fully express my appreciation for her constant encouragement, resilience, and devotion, which continue to inspire me every day.

I also wish to respectfully honor the memory of my **father**. I am deeply grateful for his love, values, and guidance, which remain with me and continue to shape the person I am today. This work stands as a tribute to his memory and influence in my life.

To my beloved sisters, **Maral and Jeyran**, thank you for your constant support, understanding, and encouragement. Your presence, care, and belief in me have been a source of strength throughout this journey. This work is dedicated to my family, whose patience, love, and support form the foundation of all my achievements.

This master's journey in Finland has been filled with growth, resilience, and unforgettable moments, all of which will remain with me long after this chapter comes to an end.

Ghazal Askari

Åbo, December 2025.

Abstract

Title of the thesis:	N_2O Decomposition Reaction over Cu modified ZSM-5, SAPO-34 and SAPO-41 Zeolite Catalysts: Effects of Oxygen Concentration and Hydrothermal Stability.

Author:	Ghazal Askari
Thesis supervisors:	Professor Dmitry Yu. Murzin, Docent Narendra Kumar, Docent Kari Eränen
	Laboratory of Industrial Chemistry and Reaction Engineering
	Johan Gadolin Process Chemistry Centre
Date and place:	December 2025, Åbo Akademi University, Turku Finland

---

One of the largest contributors to global warming and the destruction of the Earth's protective ozone layer is nitrous oxide ($\boldsymbol{N_2O}$). It has a Global Warming Potential approximately 300 times larger than carbon dioxide when measured on a 100-year time scale. Although Nitrous Oxide concentrations in the atmosphere are very low, it is generated in large quantities in many different types of industries including production of nitric acid via catalytic oxidation of ammonia and in waste treatment systems. The difficulty in controlling these emission sources and the high costs associated with developing new and effective methods for reducing Nitrous Oxide emissions have made finding a cost-effective solution an imperative necessity.

This thesis provides a method for addressing the challenge by a detailed investigation of the direct catalytic decomposition of nitrous oxide to produce nitrogen and oxygen, which are both environmentally benign compounds, over copper modified zeolite catalysts. The focus of the research is on the catalytic activities of Cu-modified ZSM-5, SAPO-34 and SAPO-41 zeolite catalysts. A major component of the research involves identifying the effects of oxygen concentration and hydrothermal reaction conditions on catalytic activity, intrinsic efficiency and long-term stability of the zeolite catalysts. To achieve this goal, the research combines several areas of study; namely, catalyst synthesis, advanced physicochemical characterization and catalytic evaluation under relevant industrial conditions to determine the limitations that affect the performance of the catalysts and to develop strategies to overcome them.

Results obtained during the research demonstrated that Cu-H-ZSM-5 exhibited much higher $\boldsymbol{N_2O}$ conversion rates and turnover frequencies than Cu-SAPO based catalysts, and thus, achieved nearly 100% conversion at temperatures larger than 400°C. Oxygen was shown to decrease the rate of $\boldsymbol{N_2O}$ decomposition due to kinetic limitations resulting from the accumulation of surface oxygen rather than the degradation of the zeolite catalyst structure. Furthermore, the research indicated that Cu-ZSM-5 has a better ability to withstand exposure to oxygen rich feedstocks than did Cu-SAPO-34 and Cu-SAPO-41, suggesting that the type of zeolite framework and the stabilization of the copper sites played significant roles in maintaining the catalytic activity. Finally, the research demonstrated that Cu-ZSM-5 is able to maintain a significant fraction of its activity in the presence of high steam concentrations and

therefore exhibits a high degree of resistance to sintering and zeolite framework structure collapse.

By elucidating the relationships between the zeolite structure, copper nanoparticle size distributions, dispersion, oxygen inhibition, and hydrothermal stability, this study advances the understanding of $\boldsymbol{N_2O}$ decomposition under realistic operating conditions. The findings contribute to the rational design of durable and efficient Cu-based zeolite catalysts and represent a meaningful step toward the development of practical catalytic technologies for long-term industrial $\boldsymbol{N_2O}$ emission control.

LIST OF SYMBOLS

He	Helium
N_2O	Nitrous Oxide
N_2	Nitrogen
O_2	Oxygen
NH_3	Ammonia
CO_2	Carbon dioxide

Greek Letters

µ	micro
µmol	micromole

Abbreviations

EIM	Evaporation impregnation
IX	Ion exchange
DP	Deposition precipitation
BAS	Brønsted acid sites
LAS	Lewis acid sites
FTIR	Fourier transform infrared spectroscopy
SEM	Scanning electron microscopy
TPD	Temperature programmed desorption
TOS	Time on stream
wt%	Weight percentage
X	Conversion
EFA	Extra-framework ammonia
TOF	Turnover frequency
TOF_{ta}	Turnover frequency in terms of total acidity
TOF_{ml}	Turnover frequency in terms of metal loading
PSD	Particle size distribution

TABLE OF CONTENTS

Table of Contents

List of Figures

List of Tables

Chapter1: Introduction

Nitrous oxide (N_2O) is recognized as a major environmental issue of our time. It is not just a powerful greenhouse gas but also the foremost ozone-depleting emission agent of the 21st century. The atmospheric concentration of N_2O has consistently risen from the pre-industrial period, attaining roughly 336 ppb in 2023, signifying a 124% increase relative to the pre-industrial baseline [2]. Nitrous oxide (N_2O) differs from other greenhouse gases such as carbon dioxide (CO_2) and methane (CH_4), which are primarily regulated by climate agreements. N_2O serves a dual role by contributing to climate forcing and promoting stratospheric ozone depletion [1,4].

The efficacy of N_2O as a greenhouse gas stems from its elevated radiative efficiency and extended atmospheric longevity. Over a century, the global warming potential (GWP) of N_2O is estimated to be around 273–310 times that of CO_2 [1,4]. Furthermore, its atmospheric longevity surpasses 110 years, indicating that once released, N_2O endures for over a century. N_2O in the stratosphere undergoes photolysis, yielding reactive NO radicals that catalyze ozone depletion through chain reactions [1,4].

The origins of anthropogenic N_2O are varied. Agriculture is the predominant source, accounting for approximately 60% of world emissions, primarily due to the utilization of nitrogen fertilizers and the management of manure [4]. Although industrial sources have a smaller overall volume, their concentration makes them appealing candidates for end-of-pipe treatment. Such processes as nitric acid and adipic acid synthesis emit exhaust gas streams with N_2O values ranging from 300 to 3500 ppm [1]. In heavy-duty diesel engine systems, N_2O is produced primarily from the combustion of fossil fuels and from after treatment processes, in particular during the NH_3 selective catalytic reduction ($4NO + 4NH_3 + O_2 \rightarrow 4N_2 + 6H_2O$) [34]. Combustion of fossil fuels, waste incineration, and wastewater treatment contribute considerably to N_2O emissions [4]. In the absence of substantial action, global N_2O emissions are anticipated to roughly triple by 2050, jeopardizing worldwide climate agreements and efforts to restore the ozone layer [2].

Among the potential mitigation strategies, direct catalytic decomposition of N_2O using metal modified catalytic materials has emerged as one of the most promising methods. In contrast to selective catalytic reduction (SCR), which necessitates the incorporation of reducing chemicals such as ammonia or hydrocarbons, catalytic breakdown directly transforms N_2O into nitrogen

and oxygen ($N_2O \rightarrow N_2 + ½ O_2$). This reaction is thermodynamically advantageous at moderate to elevated temperatures and does not necessitate any co-reductant [5,7].

A diverse array of catalysts has been evaluated for this process, encompassing noble metals, transition metal oxides, and metal-exchanged zeolites [4]. Noble metals such as Rh and Ru exhibit significant intrinsic activity; yet, their elevated cost and vulnerability to poisoning by water vapor and oxygen considerably restrict their commercial use [4]. Transition metal oxides such as cobalt and iron, in perovskite or spinel configurations, have been investigated; nevertheless, they frequently exhibit inadequate hydrothermal stability [4].

Transition metal modified zeolites, especially those including copper or iron, have garnered significant interest as effective catalysts for N_2O decomposition. These materials provide a distinctive amalgamation of structural tunability, acidity, elevated surface area, and redox-active spots [1, 2]. Copper-exchanged ZSM-5 (Cu–ZSM-5) zeolite catalyst is particularly significant due to the presence of Cu^{2+} ions within the microporous MFI framework, which can activate the N–O bond in N_2O. Research indicates that dicopper sites ($[Cu–O–Cu]^{2+}$, $[Cu–O_2–Cu]^{2+}$) are pivotal in this mechanism by promoting bond cleavage and subsequent oxygen recombination [7]. Nonetheless, despite its remarkable performance under optimal laboratory settings, Cu–ZSM-5 has significant hydrothermal instability [5,6]. Exposure to high-temperature steam causes dealumination of the zeolite structure, while copper ions move and aggregate into inactive CuO clusters, leading to fast deactivation [6,7].

This thesis concentrates on enhancing N_2O decomposition efficiency by methodically examining the impacts of oxygen content, and hydrothermal stability. Recent reviews indicate that catalyst deactivation is significantly affected by oxygen partial pressure, hydrothermal stress, and surface oxygen buildup, which modify the structural and electronic characteristics of active sites [1, 2]. Elevated O_2 concentrations can hinder the development of oxygen vacancies and decelerate the regeneration of reduced metal centers essential for N_2O dissociation. Simultaneously, hydrothermal aging promotes sintering of metal nanoparticles, dealumination (in zeolites), phase segregation, structural distortions or the depletion of redox-active surface sites. The stability issues are especially significant for industrial exhaust streams, which typically comprise 2–12% O_2 and considerable water vapor. Therefore, understanding the impact of oxygen concentrations and hydrothermal conditions on catalytic architectures and reaction pathways is crucial for the development of advanced N_2O decomposition catalysts suitable for sustained industrial use. This study aims to contribute to the innovative design of

transition metal modified catalysts that exhibit enhanced durability and performance under industrially relevant conditions by examining these factors.

Chapter 2: Literature Review

2.1 Thermodynamics of N_2O Decomposition

N_2O is the third most important greenhouse gas after CO_2 and CH_4 in terms of radiative forcing [2]. With a 100-year GWP of 310 relative to CO_2, it is among the most potent greenhouse gases [1,4]. Its radiative forcing has been increasing steadily, contributing approximately 0.2 W m^{-2} in 2020 [2]. In the stratosphere, N_2O photolysis produces NO radicals that drive ozone depletion cycles [4]. Nitrous oxide (N_2O) is a linear asymmetric N–N–O molecule in which the bond orders of the N–N and N–O linkages differ significantly, resulting in preferential cleavage of the weaker N–O bond during thermal or catalytic activation. In its uncatalyzed form, the decomposition of N_2O begins only at temperatures above 800 °C because the intrinsic activation energy for N–O bond breaking is approximately 250 kJ mol^{-1}. The global reaction describing the direct decomposition of nitrous oxide is given in Eq. 1:

$$2N_2O \rightarrow 2N_2 + O_2 \qquad \textbf{(Eq.1)}$$

This reaction is exothermic ($\Delta H°(298K) \approx -163$ kJ mol^{-1}) but kinetically hindered due to the formation and removal of surface oxygen species on catalyst active sites. Catalytic systems such as Fe- and Cu-exchanged zeolites, Co_3O_4-based oxides, CeO_2-supported copper species, and porous frameworks including ZIF-derived Co/CoO_x structures can significantly reduce the activation barrier to 50–160 kJ mol^{-1} and shift the decomposition temperature to 300–500°C. Mechanistic insights from SCR– N_2O pathways show that N_2O first adsorbs onto a redox-active metal center (M*), undergoes N–O bond scission to yield N_2 and an adsorbed oxygen atom (O*), after which O* recombines or migrates to produce O_2—a step often regarded as rate-determining. According to the literature on catalytic SCR, Cu ions are engaged in reversible redox cycles (Cu^{2+}/Cu^{+}) that activate N_2O and liberate oxygen [1,35].

2.2 Catalysts for Direct N_2O Decomposition

Researchers have focused on the catalytic decomposition of nitrous oxide (N_2O) over the past several decades, using many different types of materials. The most studied catalysts include noble metals, transition-metal oxides, and zeolite-based systems. Each type of catalyst exhibits specific benefits and drawbacks regarding catalytic performance, heat and steam resistance, tolerance to other gases in the reaction stream, and overall suitability for industrial applications.

2.2.1 Noble metal catalysts

Rhodium (Rh), ruthenium (Ru), palladium (Pd), and iridium (Ir) are all noble metals that have been demonstrated to be highly effective at decomposition N_2O. They usually achieve close to 100% N_2O conversion at relatively low temperatures (200–400 °C), which is much better than most transition metal-based systems in terms of intrinsic activity [2]. Ru supported on alumina, for instance, is quite active, while Rh-based catalysts are very selective for the direct decomposition route. However, noble metals have numerous problems. Because they are rather expensive, large-scale manufacturing and implementation are extremely challenging. They are also likely to stop working when common exhaust gas components such as oxygen (O_2), water vapor (H_2O), and sulfur oxides (SO_x) are present [7]. Ru catalysts, especially, sinter quickly when exposed to hydrothermal conditions, which makes them lose their activity and dispersion permanently. These restrictions have led researchers to look for more stable, highly efficient and plentiful alternatives based on transition metals for N_2O decomposition.

2.2.2 Transition metal oxide catalysts

Transition metal oxides, especially those containing cobalt, iron, and manganese, have garnered significant attention for the decomposition of N_2O, attributed to their affordability, environmental friendliness, and redox adaptability. Cobalt oxides, including Co_3O_4, exhibit remarkable activity, achieving conversions that surpass 80% within the temperature range of 400–500 °C [8]. Iron oxides that are supported by carriers with high surface areas demonstrate significant activity; however, they typically necessitate elevated operating temperatures in comparison to cobalt catalysts [2]. The catalytic efficacy of these oxides is significantly affected by the mobility of lattice oxygen, which dictates the kinetics of oxygen atom recombination and subsequent desorption as O_2 from decomposed N_2O. Mixed metal oxides, including perovskites such as $LaCoO_3$ and $LaFeO_3$, are attractive due to their superior capabilities in oxygen storage and redox cycling [9]. Nevertheless, transition metal oxides supported catalysts typically exhibit a deficiency in hydrothermal durability. Upon exposure to water vapor at elevated temperatures, these materials experience surface restructuring, sintering, structural distortions and a reduction in oxygen mobility, culminating in rapid deactivation during the catalytic N_2O decomposition reaction.

2.2.3 Zeolite-based catalysts

2.2.3.1 Structure and Classification of Zeolites

Zeolites are crystalline aluminosilicate frameworks composed of TO_4 tetrahedra (T = Si, Al), linked through shared oxygen atoms to form three-dimensional networks characterised by cages, channels, and rings of molecular dimensions. Their topologies are systematically classified by the International Zeolite Association (IZA). Each framework is assigned a three-letter code such as MFI (ZSM-5), CHA (SSZ-13/SAPO-34), AFO (SAPO-41), FER, MOR, BEA, FAU, etc. Structural descriptions, topology formation, and the systematic enumeration of secondary building units are extensively discussed by Yu and Li (2014) [36].

Zeolites are typically categorized by pore openings:

- Small-pore zeolites (8-membered rings), e.g., CHA
- Medium-pore zeolites (10-membered rings), e.g., MFI
- Large-pore zeolites (12-membered rings), e.g., FAU

Framework density, Si/Al ratio, pore dimensionality, and channel geometry fundamentally determine adsorption, ion exchange, and catalytic behavior.

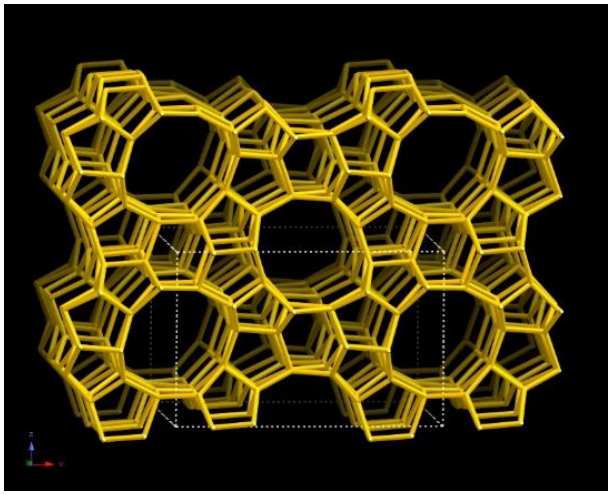

Figure 1: Framework structure of ZSM-5 zeolite (MFI topology) [55].

2.2.3.2 Acidity in Zeolites

Zeolites exhibit two primary categories of acidity that govern their catalytic behavior. Brønsted acid sites originate from isomorphic substitution of Si^{4+} by Al^{3+}, which introduces a negative

framework charge compensated by a proton, producing the canonical Si–OH–Al bridging hydroxyl; these sites display stronger acidity as the Si/Al ratio decreases and as local tetrahedral distortion intensifies. Lewis acid sites, by contrast, arise from extra-framework aluminum species formed through steaming or dealumination, as well as from coordinatively unsaturated exchanged metal cations such as Cu^{2+} or Fe^{3+}. The relative abundance and strength of these Brønsted and Lewis sites critically dictate adsorption phenomena and transition-state stabilization, thereby shaping the kinetics and mechanism of redox processes, including N_2O decomposition [36, 37].

2.2.3.3 Ion-Exchange Properties

Zeolite ion exchange arises from the framework's negative charge generated by aluminium substitution, with exchangeable cations such as Na^+, H^+, Cu^{2+}, and Fe^{3+} residing in channels and cages where they interact strongly with framework oxygens. This exchange can be carried out through aqueous ion exchange, solid-state ion exchange (SSIE), or impregnation, and the chosen method substantially affects the resulting metal oxidation state, site distribution, metal nanoparticle size and redox properties. Armandi et al. (2019) showed that aqueous ion exchange produces highly dispersed Cu^{2+} sites, impregnation leads to the formation of oligomeric CuxOy species, and SSIE generates isolated Cu^+ ions that exhibit superior stability [37].

2.2.3.4 Hydrothermal and Structural Stability

Zeolite stability is controlled by the concentration of framework aluminium, the geometry of the pore network, and the extent of exposure to steam, with high-alumina materials being especially susceptible to dealumination that results in loss of Brønsted acidity, generation of Lewis-acidic EFAL species, migration, changes in structures and agglomeration of metal ions, and eventual collapse of microporosity. As highlighted in Védrine's analysis of active-site dynamics, these structural changes occur concurrently with continuous restructuring of oxide supports, evolution of metal–support interactions, and the formation and disappearance of transient reaction intermediates under operating catalytic conditions [37].

In summary, transition metals supported on zeolites, particularly copper- and iron-exchanged variants, are among the most promising catalysts for the decomposition of N_2O. Copper-exchanged ZSM-5 (Cu–ZSM-5) is the most extensively studied catalyst, noted for its high activity and structural tunability. The zeolite framework creates distinct microporous environments that stabilize isolated or binuclear Cu^{2+} ions, which are efficient in activating the

N–O bond in N_2O [6]. Dicopper oxo-bridged species ([Cu–O–Cu]$^{2+}$) have been identified as the principal active sites that can abstract oxygen from N_2O and enable subsequent O_2 recombination [6].

Zeolite-based catalysts, despite exhibiting high intrinsic activity, encounter significant challenges in practical applications. Palella et al. (2003) found that Cu–ZSM-5 nearly completely loses its activity following hydrothermal treatment with steam, while CuAPSO-34 maintains both its crystallinity and catalytic function [4]. The observed instability is ascribed to the dealumination of the zeolite framework and the migration of Cu^{2+} into inactive CuO clusters [5]. Various strategies have been suggested to enhance hydrothermal stability, such as rare earth co-exchange (e.g., La, Ce, Sm), hierarchical structuring, and surface modification [10,11]. Recent studies have focused on nitridation and other post-synthetic modifications to enhance metal-support interactions and inhibit copper migration.

2.2.4 Structural Characteristics of SAPO Molecular Sieves

2.2.4.1 Structure and Classification of SAPOs

Silicoaluminophosphates (SAPOs) are crystalline microporous substances obtained from aluminophosphate ($AlPO_4$) frameworks through the isomorphic substitution of silicon. Their structures consist of interconnected TO_4 tetrahedra (T = Al, P, Si), creating organized pore systems with molecular-scale dimensions. The addition of silicon induces Brønsted acidity, rendering SAPOs efficient solid acid catalysts.

SAPO materials can crystallize in a wide variety of zeolite-related framework topologies, each defined by unique pore sizes (8-, 10-, or 12-membered rings), cage systems, and channel dimensionalities (1D, 2D, or 3D). Because of this structural diversity, SAPOs enable highly selective catalysis and adsorption processes. The specific framework type determines the diffusion constraints, shape selectivity, and overall catalytic behavior [39].

2.2.4.2 Structure and Properties of SAPO-34

SAPO-34 is known to crystallize in the CHA (chabazite) framework. It is known for its small-pore, cage-based structure. The CHA topology has CHA cages with internal diameters of about

1.0 nm and 8-membered ring openings of about 0.38 nm. This makes a three-dimensional network with narrow openings that connect the cages. The restricted pore structure of SAPO-34 provides pronounced shape-selective properties, which enables efficient diffusion and transformation of small molecules. Silicon is usually added to the framework as isolated substitution sites. This makes the Brønsted acidity higher, elevating catalytic activity[40].

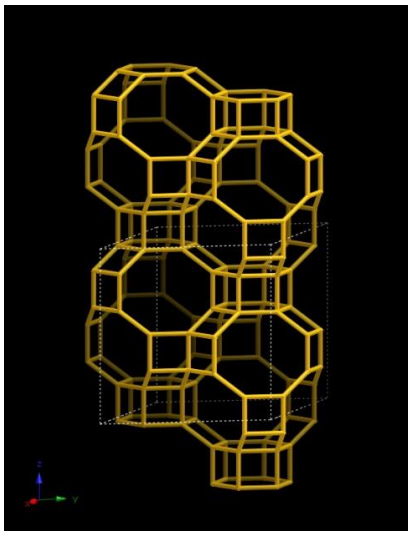

Figure.2: Framework structure of SAPO-34 (CHA topology) showing CHA cages and 8-membered ring apertures [55].

2.2.4.3 Structure and Properties of SAPO-41

SAPO-41 crystallizes with the AFO framework, distinguished by a medium-pore topology initially described in the development of aluminophosphate molecular sieves, subsequent to the pioneering work of Lok et al. (1982). The AFO structure contrasts with the cage-based confinement observed in SAPO-34, exhibiting one-dimensional, non-intersecting channels defined by 10-membered ring (10-MR) elliptical pore apertures with a free aperture of roughly 0.43 × 0.70 nm (Fig. 3). The AFO structure has non-intersecting 10-MR channels with elliptical pore apertures measuringQ 0.43 × 0.70 nm, establishing a moderately open microporous environment for heteroatoms such as silicon or transition metals. Mériaudeau et al. (1998) discovered that SAPO-41 may be produced in both silicon-deficient and silicon-excess forms, contingent upon synthesis conditions, including surfactants. The incorporation of dodecylamine yields smaller crystals (0.2-0.5 μm) and enhances silicon substitution, whereas conventional syntheses produce larger pseudo cylindrical crystals (2-5μm) with reduced silicon incorporation. An MAS NMR structural study reveals that low-silicon SAPO-41 contains isolated Si(4Al) sites, whereas silicon-rich materials exhibit a broader spectrum of Si(nAl)

environments and contributions from silica domains. These variations directly influence Brønsted acidity, as demonstrated by NH_3-TPD and IR spectroscopy. Silicon-rich SAPO-41 possesses a reduced number of Si(OH)Al acid sites, although it exhibits more robust Brønsted sites in proximity to silica–alumina intergrowth regions as a result of silicon substitution. Physicochemical characteristics, including framework topology, channel geometry, silicon-dependent acidity, and adjustable crystallite shape and size, are essential for comprehending metal-modified SAPO-41 materials, particularly regarding Cu species, size, dispersion and redox capabilities for catalytic N_2O decomposition reaction $[39-41]$.

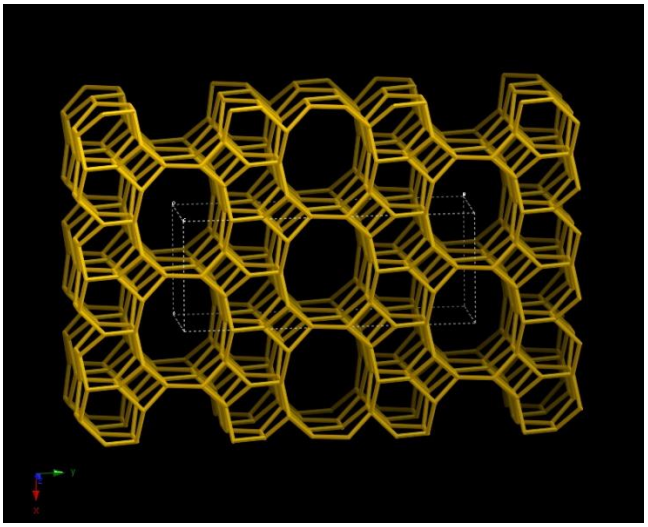

Figure.3: Framework structure of SAPO-41 (AFO topology) showing 1D 10-MR elliptical channels [55].

2.3 Mechanism of N_2O Decomposition

Although the catalytic decomposition of nitrous oxide (N_2O) into nitrogen(N_2) and oxygen (O_2) appears to be a straightforward reaction (Eq. 2), the underlying mechanism is extremely intricate and heavily reliant on the type of catalyst, the structure of the active site, oxidation state, metal nanoparticle size and the reaction environment.

$$N_2O \rightarrow N_2 + \frac{1}{2} O_2 \qquad \textbf{(Eq.2)}$$

A consensus has been reached regarding the overall process, which occurs in sequential steps: (i) adsorption and activation of N_2O, (ii) cleavage of the N–O bond with the release of N_2, (iii) accumulation of surface oxygen species, and (iv) recombination and desorption of O_2. The rate-determining step (RDS) is typically linked to the processes of oxygen recombination or desorption from the catalyst surface.

2.3.1 N_2O Adsorption and Activation

First, N_2O adsorbs on a redox-active site, usually a metal–oxygen vacancy or transition metal cation. This adsorption step forms an activated N2O species on the catalyst surface. Studies using density functional theory (DFT) showed that, in contrast to isolated mononuclear sites, dicopper oxo species ($[Cu–O–Cu]^{2+}$) or dinuclear Fe sites in zeolites reduce the activation barrier for N–O bond cleavage [1,6].

2.3.2 Oxygen Recombination and Desorption

After N_2 release, the residual O* atom occupies the active site. For the catalyst to maintain its cycling, the O* must desorb as O_2. Two pathways are generally recognized.

- **Langmuir–Hinshelwood (L–H) mechanism:** Two adjacent O* atoms recombine to form O_2.

$$2O^* \rightarrow O_2 + 2* \qquad \textbf{(Eq.3)}$$

- **Eley–Rideal (E–R) mechanism:** A gas-phase N_2O molecule reacts directly with a pre-adsorbed O*.

$$N_2O(g) + O^* \rightarrow N_2(g) + O_2(g) + * \qquad \textbf{(Eq.4)}$$

The L–H mechanism dominates when active sites are closely spaced, while the E–R pathway is more relevant on catalysts with isolated sites [1]. In both cases, O_2 desorption is the RDS, as surface O atoms bind strongly to transition metals and oxides.

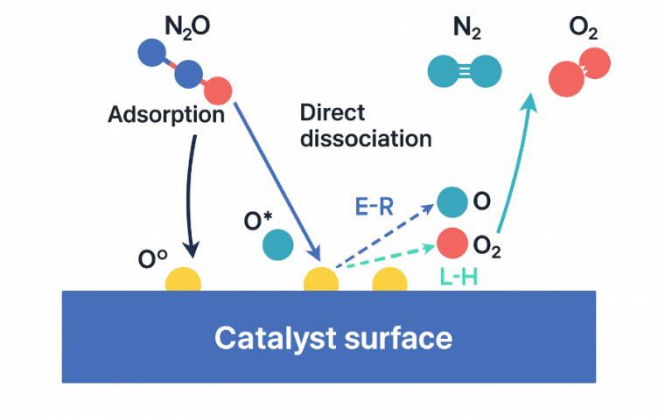

Figure.4: E-R and L-H mechanisms for the catalytic decomposition of N_2O to N_2 and O_2 [1].

2.3.3 Influence of Catalyst Structure on N_2O Decomposition Reaction Mechanism

The catalytic mechanism exhibits significant sensitivity to the local structure of active sites. Studies utilizing DFT and operando techniques indicate that binuclear Fe species in SSZ-13 exhibit larger activity than monomeric Fe, attributed to their capacity to stabilize O–O bond formation. Conversely, the presence of Fe nanoparticles in SAPO-34 is associated with aggregation, which results in decreased N_2O decomposition activity [1].

Cu-based zeolites with isolated $ZCuOH$ species promote side reactions, resulting in N_2O formation during SCR processes, while Z_2Cu sites enhance the effective decomposition of N_2O [12,1].

Co-based oxides facilitate N_2O activation through Co^{3+}/Co^{2+} redox pairs and oxygen vacancies, with the mobility of lattice oxygen serving as a crucial determinant [13]. The Cu/CeO_2 catalyst has binuclear [Cu–O–Cu] active sites. The presence of Cu^{2+} species on ceria nanorods demonstrates remarkable catalytic activity, attributed to the synergistic redox cycling of Cu^{2+}/Cu^{+} and Ce^{4+}/Ce^{3+} [14].

Porphyrin-based catalysts: Density Functional Theory indicates that Ti–porphyrins facilitate N_2O decomposition via multi-cycle oxygen transfer, with O_2 desorption barriers determining the overall reaction rates [15].

2.3.4 Inhibition of N_2O Decomposition Reaction by O_2, H_2O, and NO

Exhaust streams with high levels of oxygen, water vapor, and nitrogen oxides hinder N_2O breakdown.

- O_2 inhibition: Oxygen competes with N_2O for adsorption, stabilizes O^*, and increases O_2 desorption barrier [16,1].
- H_2O inhibition: It occurs when water forms hydroxylated intermediates (e.g., [Cu–OH–Cu]), deactivating N_2O activation sites [6,17].
- NO inhibition: NO and NO_2 can occupy active centers or react with surface oxygen intermediates, causing NO_x generation instead of O_2 release [18].

These inhibitory mechanisms demonstrate the challenges of creating N_2O decomposition catalysts that are cost effective, active and stable in hydrothermal and oxidizing conditions.

Chapter 3: Experimental

3.1 Materials and Chemicals

Copper(II) nitrate trihydrate ($Cu(NO_3)_2 \cdot 3H_2O$, ≥ 99%, Sigma-Aldrich) and copper(II) acetate monohydrate ($Cu(CH_3COO)_2 \cdot H_2O$, ≥ 99%, Merck) were employed as metal precursors. Commercial ammonium-form ZSM-5 zeolite (SiO_2/Al_2O_3 = 50, CBV 5524 G, Zeolyst International) was used as the parent support. Deionized water (18.2 MΩ cm) was used in all syntheses. High-purity gases—nitrous oxide (N_2O ≥ 99.9%), helium (He ≥ 99.999%), oxygen (O_2 ≥ 99.999%)—were supplied by AGA Finland.

All chemicals were used as received without further purification. The prepared catalysts are denoted as Cu–HZSM-5(50) and Cu–NIT–HZSM-5(50), where "NIT" refers to nitrite copper species as Cu precursor, introduced via post-synthetic modifications.

For SAPO materials, phosphoric acid (H_3PO_4, 85%, Merck), boehmite (AlOOH, Sasol), aluminium isopropoxide ($Al(O\text{-}iPr)_3$, Merck), fumed silica (Aerosil), and colloidal silica (Ludox LS-40, 40 wt%) were used as P, Al, and Si sources. Morpholine, tetraethylammonium hydroxide (TEAOH), and di-n-propylamine (all ≥ 99%, Sigma-Aldrich) served as organic templates in the SAPO-34 and SAPO-41 syntheses. Deionized water (18.2 MΩ·cm) was used in all preparations.

3.2 Preparation of Catalysts

The method employed to incorporate copper species into the zeolite framework significantly influences the catalyst's dispersion, oxidation state, and stability. Various established methods for synthesizing Cu–ZSM-5 and SAPO-34 and SAPO-41 catalysts include ion exchange (IEM), deposition-precipitation (DP), co-precipitation (CP), and evaporation impregnation (EIM). This study employed the EIM method.

3.2.1 Evaporation Impregnation Method (EIM)

Synthesis of Cu-ZSM-5, Cu-SAPO-41, and Cu-SAPO-34 catalysts applied EIM. This method achieves uniform dispersion of metal ions within the zeolite framework and ensures strong metal–support interactions, consistent with findings of Kim et al. [19].

The evaporation impregnation method is one of the most common techniques for placing active metals onto supports, and it is carried out in the liquid phase.

For preparing metal modified zeolite catalysts using Evaporation Impregnation Method (EIM), copper nitrate was used as the metal precursor. First, 3.56 g of the copper nitrate precursor was dissolved in 250 mL of deionized water, and the pH of the solution was measured. Then, 10 g of the support material—various types of SAPO and ZSM-5 zeolite—was added, and the pH was measured again. The mixture was stirred well to make sure the support was fully dispersed in the solution.

The suspension was then placed in a Büchi rotary evaporator (Büchi rotavapor R-114) and rotated overnight at 60°C at 100 rpm. After 24 hours, water evaporated under vacuum. The solid product was collected and dried in an oven at 110°C for 24 hours. Finally, the dried solid was calcined in a muffle oven using step calcination procedure to produce the final catalyst.

During the synthesis of Cu-SAPO-41, for example, the initial pH after adding 3.56 g of copper nitrate to 250 ml deionized water was 4.11. After adding 10 g of SAPO-41 zeolite, the pH dropped to 3.64, reflecting acidic intrinsic of the SAPO-41 zeolite.

The catalysts were labeled as Cu-ZSM-5(EIM), Cu-SAPO-34 (EIM), Cu-SAPO-41 (EIM).

3.2.2 Ion-Exchange Method (IEM)

Ion exchange is a common method for preparing catalysts with isolated metal sites on a solid support. Unlike methods such as EIM or deposition–precipitation, it usually gives lower metal loadings; however, providing the good control of how metal ions are introduced. In this wet-chemical process, metal ions in solution substitute the original cations on the support, including Na^+, NH_4^+, or H^+. The exchange typically occurs under stirring at room temperature or slightly elevated temperatures, and pH adjustment may be necessary to maintain the stability of metal ions in solution.

In a standard procedure, the support material is combined with an aqueous solution of the metal precursor at a specified concentration. The pH is controlled in a way that the desired metal species remains soluble and active for exchange. During the stirring process, the original cations on the support are slowly replaced by the metal ions present in the solution. After the exchange

is finished, the solid is separated by filtration, washed to remove any remaining ions or impurities, and then dried. A final calcination step is usually applied to decompose remaining salts, stabilize the metal species, and generate the active catalyst [42].

This process generates framework-associated metal species, including $[Cu–O–Cu]^{2+}$, which exhibit high activity in N_2O decomposition [20, 23]. These sites may migrate or aggregate into inactive clusters during hydrothermal treatment.

3.2.3 Deposition–Precipitation Method (DP)

The deposition–precipitation (DP) method is widely used to prepare supported metal catalysts with high dispersion and loadings. In this technique, a metal precursor dissolved in a solution is selectively precipitated onto the surface of a solid support by controlling pH and temperature. The goal is to avoid bulk precipitation and ensure that nucleation occurs mainly on the support surface, which leads to a uniform distribution of the active phase [43].

During synthesis, the support is suspended in the precursor solution, and a precipitating agent is slowly introduced to maintain the metal concentration between solubility and super-saturation limits. After deposition, the solid is filtered, washed, and then calcined or reduced to obtain the final active sites. Surface functional groups play an important role by providing anchoring sites that enhance metal–support interactions and improve the hydrothermal and catalytic stability of the catalyst [43].

The DP method offers an effective strategy for producing supported catalysts that exhibit controlled particle size and robust interactions between the active phase and the support, rendering it appropriate for applications that demand high stability and efficiency [22, 43].

3.2.4 Co-precipitation Method (CP)

The co-precipitation (CP) method is one of the most widely applied techniques for preparing heterogeneous catalysts due to its simplicity and cost-effectiveness. It involves the simultaneous precipitation of multiple metal ions from a solution by adjusting the pH to reach the solubility limit of the metal salts. This produces mixed hydroxides or basic salts that can later be transformed into the desired oxide materials after drying and calcination.

During CP, metal salts are dissolved in a solution and a precipitating agent is added under controlled stirring. Nucleation occurs once supersaturation is achieved, followed by crystal

growth at the solid–solution interface. The final particle size depends on the relationship between nucleation and growth rates. Maintaining a constant pH is recommended because it leads to uniform precipitation and better control of composition. In contrast, variable-pH precipitation may result in uneven distribution if different cations precipitate at different pH ranges.

Operational factors such as the precursor type, pH, temperature, ageing time, and mixing rate influence the structure, morphology, and dispersion of active phases in the final catalyst. Proper washing and removal of residual ions are also required to prevent contamination or catalyst poisoning. After precipitation, the solid is separated, washed, dried, and calcined to form a stable catalytic phase.

Overall, co-precipitation is a practical and efficient route to obtain homogeneous mixed-oxide catalysts with controlled textural properties, making it suitable for various industrial catalytic applications [21].

3.3 Catalyst Calcination and Activation

All produced catalysts underwent a regulated calcination procedure to eliminate remaining precursor species and form the active catalytic phase. The treatment began at ambient temperature and was gradually elevated to 250°C over a period of 75 minutes. The temperature was maintained at a constant level for 60 minutes to facilitate adequate decomposition of surface ligands. The system was subsequently heated to 400°C over a period of 45 minutes and held at that temperature for 180 minutes to achieve complete calcination. The materials were subsequently cooled to room temperature over a period of approximately 100 minutes to ensure structural stabilization. The stepwise calcination procedure facilitated the complete removal of metal precursor while maintaining catalyst structural integrity.

Table.1: Step calcination procedure

75 min	250℃
60 min	250℃
45 min	400℃
180 min	400℃
100 min	25℃

3.4 Physico-chemical Catalyst Characterization

The catalysts' structural and chemical characteristics were examined using the following techniques:

3.4.1 Nitrogen Physisorption

Nitrogen physisorption was used to study the textural properties of the metal modified and pristine zeolite catalysts, including the surface area, pore size, and pore volume. The N_2 adsorption measurements were carried out at 77 K using a Micromeritics MicroActive 3Flex 3500 instrument. Before the analysis, the samples were dried at 180°C under vacuum overnight and then degassed in-situ at 250°C for 4 hours to remove moisture and any adsorbed gases. The nitrogen adsorption–desorption isotherms give useful information about the pore structure. According to IUPAC, the pores are divided into micropores, mesopores and macropores. Pore classifications are typically grouped by diameter range and dominant adsorption mechanism. Micropores have diameters less than 2 nanometers and are characterized by enhanced field-induced micropore filling as the dominant adsorption mechanism. Mesopores range from 2 to 50 nanometers in diameter, where multilayer adsorption and capillary condensation predominate. Macropores are those larger than 50 nanometers and are primarily associated with transport macroporosity.Zeolite catalysts mainly show microporous behavior, which appears as a fast nitrogen uptake at low relative pressures ($p/p_o < 0.1$). This behavior is related to the strong adsorption forces inside very small pores. The specific surface area of the catalysts was calculated using the Dubinin–Radushkevich (D–R) method, which is suitable for microporous materials. The pore size distribution was obtained using the NLDFT model. In addition, the micropore volume was estimated by the Horváth–Kawazoe (H–K) method. These methods are commonly used for materials such as zeolites, where nitrogen adsorption mainly happens inside micropores rather than by forming multilayers on the surface [27, 44, 45].

Table 2: Nitrogen physisorption results of synthesized proton form, Cu modified ZSM-5, and SAPO zeolite catalysts.

Catalyst	Surface Area (Dubinin-Radushkevich) m2 /g	Total pore volume V∑, (cm^3 /g)	Micropore volume, V_{MP} (cm^3/g)	Microporosity (%)	H-K pore volume, (cm^3 /g)
H ZSM5-50	448	0.25	0.22	86	0.17
Cu (NIT) H-ZSM5-50-EIM(1.78gr)	380	0.19	0.17	89	0.14
Spent Cu (NIT) H-ZSM5-50-EIM (1.78gr)-10vol%O_2	360	0.14	0.13	92	0.13
Spent Cu (NIT) H-ZSM5-50-EIM (1.78gr)-5vol%H_2O	376	0.2	0.11	55	0.14
Spent Cu (NIT) H-ZSM5-50-EIM (1.78gr)-10vol%H_2O	367	0.12	0.05	41	0.07
Spent Cu (NIT) H-ZSM5-50-EIM (1.78gr)-15vol%H_2O	334	0.23	0.08	34	0.12
Cu (NIT) H-ZSM5-50-EIM(3.65gr)	370	0.21	0.1	47	0.13
Spent CU NIT H-ZSM5-50-EIM (3.56gr)- 5vol%H_2O	488	0.29	0.13	44	0.18
Spent CU NIT H-ZSM5-50-EIM (3.56gr)- 10vol%H_2O	202	0.12	0.05	41	0.07
Spent CU NIT H-ZSM5-50-EIM (3.56gr)- 15vol%H_2O	358	0.23	0.08	34	0.14
Cu- SAPO-41	56	0.25	0.001	0.4	0.02
Spent Cu-SAPO-41-10vol%O_2	48	0.2	0.008	4	0.017
Spent Cu -SAPO-41-5vol%H_2O	46	0.2	0.009	4.5	0.016

Spent Cu -SAPO-41-10vol%$\boldsymbol{H_2O}$	47	0.2	0.008	4	0.017
Spent Cu -SAPO-41-5vol%$\boldsymbol{H_2O}$	51	0.23	0.005	2.17	0.019
Cu- SAPO-34	1	0.0006	0	-	0.0008
Spent Cu-SAPO-34-10vol%$\boldsymbol{O_2}$	1	0.0004	0	-	0.00054
Spent Cu -SAPO-34-5vol%$\boldsymbol{H_2O}$	3	0.0067	0	-	0.0014
Spent Cu -SAPO-34-10vol%$\boldsymbol{H_2O}$	3	0.0072	0	-	0.0014
Spent Cu -SAPO-34-15vol%$\boldsymbol{H_2O}$	3	0.008	0	-	0.0013

3.4.2 Transmission Electron Microscopy (TEM)

Transmission Electron Microscopy (TEM) using a JEM-1400 Plus Transmission Electron Microscope was utilized to analyze the morphology and measure metal nanoparticle size distribution (PSD) of the synthesized catalytic materials. TEM offers direct, high-resolution visualization of nanoscale features, facilitating precise evaluation of particle dimensions and structural organization. Before imaging, the samples underwent ultrasonic dispersion in ethanol to reduce agglomeration, and a single drop of the resulting suspension was placed onto a perforated carbon film supported by a copper grid for TEM observation [46]. This research employed a transmission electron microscope operating at an accelerating voltage of 110 kV and a beam current of 70 μA to attain optimal imaging conditions and resolution [28].

High-resolution micrographs were obtained to confirm the integrity of nanostructures and the Cu dispersion, as typically applied for mesoporous and nanoparticulate materials [46]. High-resolution TEM micrographs were analyzed with ImageJ software to obtain particle diameter measurements. The image scale was calibrated with the microscope scale bar, and circular nanoparticles were assessed via the direct diameter measurement or projected area conversion ($d = 2\sqrt{(S/\pi)}$) for precise sizing. Outlier values resulting from particle overlap were excluded to avoid bias in the statistical analysis [28].

The processed data were imported into Origin software, where particle sizes were categorized into bins to create a PSD histogram, with particle diameter represented on the X-axis and frequency on the Y-axis. A Gaussian fit was utilized to ascertain the mean particle diameter and standard deviation, providing a quantitative evaluation of nanoparticle size uniformity and dispersion.

3.4.3 Measurement of Brønsted and Lewis Acid Sites in Proton-, Cu-Modified ZSM-5 and SAPOs Zeolite Catalysts by FTIR spectroscopy using Pyridine as Probe Molecule

Brønsted and Lewis acid sites of the proton-exchanged zeolite catalysts were characterized using a Shimadzu IR-Trace 100 FTIR spectrometer, with pyridine employed as the probe molecule. A 10–20 mg self-supporting pellet (radius 0.65 cm) was placed in an in-situ FTIR cell and pretreated under vacuum at 450 °C for 1 h. After cooling to 100 °C, a background spectrum was collected, followed by pyridine adsorption at 100 °C for 30 min. By heating the sample step-by-step and recording the spectra after each evacuation, it was possible to identify acid sites with different strengths depending on how strongly they held the pyridine. Pyridine desorbed at 250–350 °C was attributed to weak–medium sites, 350–450 °C to medium–strong sites, and pyridine retained above 450 °C to strong sites.

IR spectra were recorded at each temperature ramp under vacuum. The characteristic vibrational bands of adsorbed pyridine for Brønsted and Lewis acid sites were monitored at 1545 cm^{-1} (associated with pyridinium ion formation, indicating proton-donating Brønsted sites) and 1450 cm^{-1} (indicative of coordinatively bound pyridine on Lewis acid sites), respectively [30].

The amount of acid sites was calculated by measuring the area of the main absorption bands and applying the Lambert–Beer law to relate these values to the concentration of adsorbed pyridine. The integrated molar extinction coefficients for adsorbed pyridine were adopted from Emeis, who determined extinction coefficients of 1.67 cm μmol^{-1} for Brønsted sites and 2.22 cm μmol^{-1} for Lewis sites under comparable experimental conditions [29]. The mass of the catalyst wafer was included in the calculation to obtain the acid site density expressed as $\mu mol\ g^{-1}$.

Pyridine-FTIR is considered a reliable method to study the acidity of zeolite catalysts because it can separate Brønsted acid sites, which donate protons, from Lewis acid sites, which accept electrons. Many studies have shown this clear distinction in pyridine-adsorbed spectra. The technique is also trusted because the measured Brønsted acidity has been found to agree with the catalytic performance of materials in typical acid-catalyzed reactions reported in the literature. Therefore, this method is useful for evaluating both the amount of acid sites and how they are distributed in protonic zeolite catalysts [30].

Table 3: Brønsted and Lewis acid in proton, Cu modified ZSM-5 zeolite catalysts using pyridine-probed FTIR.

Catalyst	Brønsted acid sites (µmol/g)				Lewis acid sites (µmol/g)				Total acid sites (µmol/g)		
	Ultra W	W	M	S	Ultra W	W	M	S	BAS	LAS	Total
Cu (NIT) H-ZSM5-50-EIM (1.78gr)-10vol%$\boldsymbol{O_2}$	0	37	43	42	619	459	298	224	122	1600	1722
Cu (NIT) H-ZSM5-50-EIM (1.78gr)-5vol%$\boldsymbol{H_2O}$	0	22	28	17	428	297	182	135	67	1042	1109
Cu (NIT) H-ZSM5-50-EIM (1.78gr)-10vol%$\boldsymbol{H_2O}$	13	22	34	19	509	363	233	168	88	1273	1361
Cu (NIT) H-ZSM5-50-EIM (1.78gr)-15vol%$\boldsymbol{H_2O}$	10	24	37	18	523	383	242	175	89	1323	1412
CU NIT H-ZSM5-50-EIM (3.56gr)-5vol%$\boldsymbol{H_2O}$	17	34	48	0	470	330	209	166	99	1175	1274
CU NIT H-ZSM5-50-EIM (3.56gr)-10vol%$\boldsymbol{H_2O}$	-	-	-	-	246	196	114	73	-	629	629
CU NIT H-ZSM5-50-EIM (3.56gr)-15vol%$\boldsymbol{H_2O}$	14	22	36	30	380	288	175	135	102	978	1080

3.4.4 SEM-EDS

Scanning Electron Microscopy (SEM) is a crucial method for examining the surface and microstructure of catalytic materials. A focused electron beam scans the sample and produces high-resolution images that show the shape, surface texture, and fine structural details of the catalyst. SEM also gives a three-dimensional appearance and has a much higher resolution than optical microscopes. This allows observation of particle size, crystal morphology, and surface defects more clearly [46].

SEM is commonly used for heterogeneous catalysts like pristine and metal modified zeolite catalysts to examine the overall morphology, shape, size, distributions of crystals and structural changes that may affect their performance. Modern SEM instruments can also analyze non-conductive materials by using low accelerating voltage to reduce charging on the surface [46].

In this work, SEM–EDS analysis was conducted using a LEO 1530 Gemini scanning electron microscope equipped with an Ultradry Silicon Drift Detector (SDD) for X-ray detection. The SEM was manufactured by LEO in Oberkochen, Germany, in 2001. The X-ray detector was produced by Thermo Scientific in Madison, Wisconsin, USA, in 2022, with model number 226D-3UPS-SN. This configuration allowed simultaneous acquisition of morphological and compositional information from the same regions of interest.

Energy-Dispersive X-ray Spectroscopy (EDX) is often attached to SEM to provide chemical composition information from the same area. It identifies the elements contained in the sample and their spatial distribution. In the case of mesoporous catalysts, EDX serves to verify the Si/Al ratio and assess the successful incorporation of aluminum into the structure, a factor that is crucial for catalytic activity [47].

The integration of SEM and EDX elucidates the correlation between surface structure and chemical composition in relation to catalyst performance. It can show if preparation methods change the surface, improve active sites, or enhance stability, which supports the development of better catalysts.

Table 4: SEM-EDS characterization results of synthesized catalysts

Catalyst	SEM - EDS Results					
	Compound %				SiO_2 /Al_2O_3	Metal loading, weight%
	Al_2O_3	SiO_2	Cu_2O	P_2O_5		
Cu (Nit)-HZSM5-50-EIM (1.78g)	3.04	91.09	5.88	-	48	5.22
Cu (Nit)-HZSM5-50-EIM (3.56g)	2.93	88.20	8.86	-	48	7.87
Cu-SAPO-41-EIM	29.30	1.93	28.82	39.94	41	25.60
Cu-SAPO-34-EIM	34.26	10.71	24.20	30.82	34	21.50

3.4.5 Temperature Programmed Reduction (TPR)

Temperature-programmed reduction (TPR) measurements were carried out using a quartz reactor connected to a Microtrac MRB BELCAT II instrument equipped with a thermal conductivity detector (TCD). This technique is used to study the reduction rates of metal oxide catalysts as a function of temperature. This technique can be used to characterize oxidative-reductive properties of both bulk and supported catalysts by evaluating the ease of their reduction with hydrogen. During TPR measurements, a gas used for reduction (for instance, H_2) continuously flows through a porous metal modified catalyst. At low temperatures, reduction is absent; however, as temperature increases, the metal oxide undergoes reduction until the reaction reaches completion. The variation in gas concentration is quantified through a detector, manifesting as peaks in the TPR curve, which indicates distinct reduction stages of the catalyst [48].

In the present work, TPR experiments were carried out with the Microtrac BELCAT II system. Approximately 0.500 g of catalyst was used, followed by pre-treatment at 200 °C for 2 hours and cooling to 50 °C. Thereafter, the sample was heated to 800 °C with a ramp of 5 °C /min under 1.5 ml/min of hydrogen and 28.5 ml/min of argon (5 vol.% hydrogen and 95 vol.% argon). When reduction of the sample took place, hydrogen was consumed, which was recorded by a thermal conductivity detector (TCD).

TPR helps to understand the redox properties of catalysts, the number of reducible species, and the temperature needed to activate the metal phase.

Because it is fast, low-cost, and simple to perform, it is widely used in catalyst characterization. The technique can also provide information about the strength of metal–oxygen bonds and the best reduction conditions for the catalyst before its use in a chemical reaction [48, 49].

Several factors can influence TPR results, including the method of catalyst preparation, particle size, metal loadings and gas flow conditions. These may cause differences in peak shape and temperature [50].

Figure 5 shows that all four synthesized Cu-containing catalysts exhibit pronounced hydrogen-consumption peaks in the temperature range of about 250–320 °C, which are associated with the reduction of highly dispersed and readily reducible Cu^{2+} species. These copper species are likely located at cation-exchange positions or finely dispersed within the ZSM-5 or SAPO zeolite frameworks. For the two Cu/HZSM-5 catalysts, both samples display main reduction peaks in this same temperature region, confirming that the nature of the copper species is essentially similar; however, the material prepared with 3.65 g copper shows a higher-intensity peak, consistent with its higher copper loading. Importantly, the Cu/HZSM-5 prepared with 1.78 g copper exhibits the main reduction peak at slightly lower temperature, indicating more easily reducible copper species and thus more favorable Cu^{2+}/Cu^{+} redox cycling. Cu-SAPO-34 also presents an intense peak in this region, suggesting highly dispersed and readily reducible copper species, whereas Cu-SAPO-41 displays, in addition to the main peak, a broad high-temperature shoulder extending up to about 700–800 °C that is attributed to more strongly interacting or less accessible CuO species. Overall, the reducibility and dispersion of copper species depend strongly on the support structure and copper loading, with the Cu/HZSM-5 (1.78 g) catalyst showing particularly advantageous low-temperature reducibility that is expected to be beneficial for N_2O decomposition reactions.

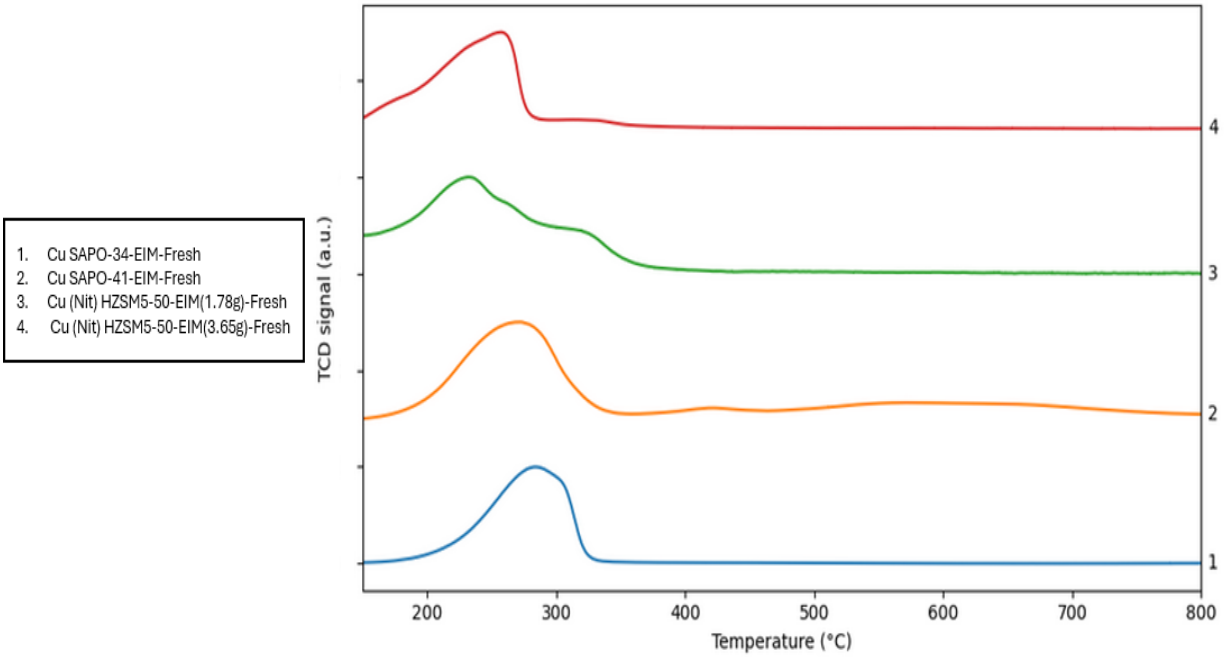

Figure 5 : H_2-TPR profiles of Cu/HZSM-5 (1.78 g and 3.65 g precursor), Cu-SAPO-34 and Cu-SAPO-41 catalysts.

3.4.6 X-ray Powder Diffraction (XRD)

X-ray powder diffraction (XRD) was used in this work to confirm that the crystalline frameworks of HZSM-5, SAPO-34, and SAPO-41 were preserved after copper modification and to check for the formation of any additional crystalline copper oxide phases. The measurements were performed using a Bruker D8 Advance X-ray diffractometer equipped with Cu Kα radiation (λ = 1.5418 Å). The diffraction patterns of the Cu-modified catalysts were compared with those of the corresponding pristine supports and with reference patterns from the JCPDS database to assess phase purity. In particular, changes in peak intensity, position, or broadening were evaluated to identify framework distortion, loss of crystallinity, or the presence of bulk CuO phases. The XRD results were therefore directly used to verify that the synthesis procedures did not damage the ZSM-5 zeolite and SAPO structures and to distinguish framework-stabilized Cu species from segregated crystalline copper oxide, which is important for interpreting the catalytic performance of the prepared materials [30, 32, 33].

3.5 Experimental Setup for Evaluation of Cu Modified ZSM-5, SAPO-41, and SAPO-34 Zeolite Catalysts in N_2O Decomposition Reaction

3.5.1 Reactor Filling:

The filling process of the stainless-steel tubular reactor is shown in Figure 6. The reactor features a heating length of 32 cm, with packing executed in multiple stages to ensure the catalyst remains stationary and gas flow is optimized. To keep the catalyst from moving during the reaction, a thin layer of glass wool is first placed at the bottom. Approximately 50% of the reactor is occupied by glass beads of 250–500 µm in size. This facilitates uniform distribution of gas. A thin layer of glass wool is applied atop the beads to provide support for the catalyst.

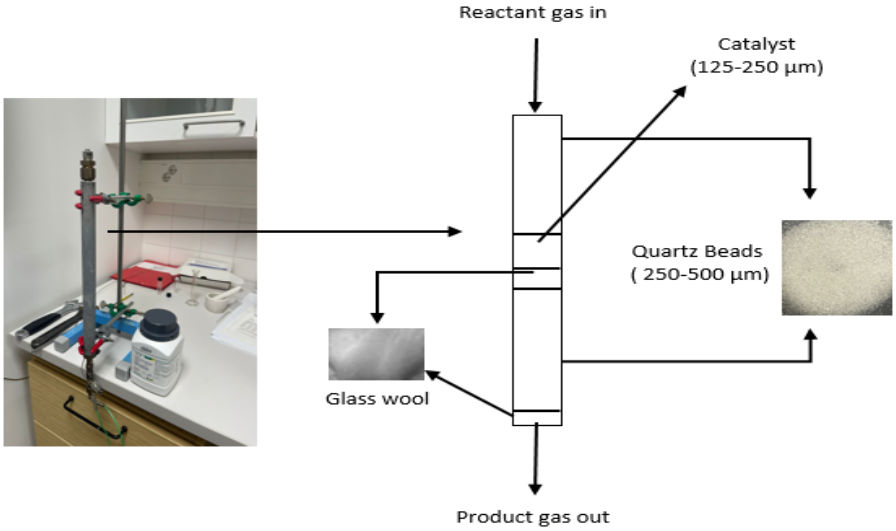

Figure 6: Tubular reactor and its layered filling

The thermocouple is subsequently inserted with its tip positioned within the catalyst bed, facilitating accurate temperature measurement. Subsequently, 0.4 g of catalyst particles, with a size range of 125–250 µm, is meticulously placed atop the support layer. The remainder of the

reactor is filled with identical glass beads as previously utilized. The gas flow enters from the top, above the upper bead layer, ensuring uniform distribution to the catalyst.

3.6 Catalytic Activity Testing

Figure 7 shows the complete experimental setup used for the N_2O decomposition tests. The gas flows of nitrous oxide, oxygen, and helium were controlled with high accuracy using Brooks Instruments mass flow controllers (MFCs) before entering the reactor system. The catalyst-filled reactor was placed inside an aluminium heating block for thermal stability. A K-type thermocouple was placed within the aluminum block so that the temperature at the catalyst bed could be monitored and precisely controlled. Heating of the reactor was provided by a Carbolite oven.

Figure 7: Experimental setup for evaluation of Cu modified ZSM-5, and SAPO zeolite catalysts in $\boldsymbol{N_2O}$ decomposition reaction.

To evaluate the hydrothermal stability of the catalyst, water was introduced into the reactor using a controlled water pump. Water was evaporated in the reaction zone, enabling the catalyst to be evaluated under steam-containing conditions. After passing through the reactor, the outlet gas stream was directed to a cooling column, where water vapor was condensed. After the water removal, the residual gas stream was directed to the gas chromatograph (HP 6890 Series) for analysis. The temperature increased from 300 °C to 500 °C at a rate of 10 °C per minute. Outlet

gases were analyzed online using an Agilent 7890A GC equipped with a thermal conductivity detector (TCD) and molecular-sieve/Porapak Q columns. The gas chromatograph also employed two columns: HP-PLOT-Q (0.53 mm internal diameter, 30 m length, 40 m film thickness) and HP-MOLSIV (0.53 mm internal diameter, 30 m length, 25 m film thickness) to guarantee efficient separation of the reaction gases. Flame ionization detector (FID) were applied for the quantification of $\boldsymbol{N_2}$, $\boldsymbol{O_2}$, and $\boldsymbol{N_2O}$. This structure permitted exact assessment of catalytic performance under conventional reaction conditions and during hydrothermal stability assessments.

3.7 Catalyst Testing

After the reactor tube was packed with the catalyst, it was connected to the experimental setup, and the catalytic tests were carried out. The reaction temperature was increased gradually from 25°C up to 500°C, using 50°C increments at each step. The corresponding temperature values and time-on-stream (TOS) measurements for all tested catalysts are provided in Appendix B. Throughout the experiments; four different reaction conditions were applied and used consistently for the entire study.

Table 5. Reaction conditions for the evaluation of Cu-modified zeolite catalysts in N_2O decomposition. The total gas flow was maintained at 200 mL min^{-1}, with an N_2O flow of 0.2 mL min^{-1} (1000 ppm) and an O_2 flow of 20 mL min^{-1}.

Conditions	**He** Flow	Water Flow
With 10vol% $\boldsymbol{O_2}$	179.8 ml/min	0
With 5vol%$\boldsymbol{H_2O}$	179.8 ml/min	10 ml/min
With 10vol%$\boldsymbol{H_2O}$	159.8 ml/min	20 ml/min
With 15vol%$\boldsymbol{H_2O}$	149.8 ml/min	30 ml/min

4 Results & Discussion

N_2O conversion (X_{N_2O}) was calculated using Equation (5):

$$Conversion\ (\%), X_{N_2O} = \frac{[N_2O]_{in} - [N_2O]_{out}}{[N_2O]_{in}} \times 100\% \qquad (\mathbf{Eq.\ 5})$$

The intrinsic catalytic activity of the synthesized samples was compared by determining the turnover frequency (TOF) for N_2O decomposition. The TOF indicates the quantity of N_2O molecules transformed per active site per unit of time. The calculations were performed using the equations presented by Gallego-Villada et al [53, 54].

Turnover frequency in terms of metal loading (TOF_{ML}) is used to assess the intrinsic activity of Cu-modified zeolite catalysts for N_2O decomposition by normalizing the reaction rate to the total amount of metal present in the catalyst.

In this work, $TOF_{ML}$was calculated using the following expression:

$$\mathrm{TOF_{ML}}(Min)^{-1} = \frac{n_{in} - n_{out}}{\Delta t \times W \times ML} \qquad (\mathbf{Eq.\ 6})$$

In this expression, $(n_{in} - n_{out})/\Delta t$ represents the number of moles of N_2O decomposed per minute, calculated from the difference between the inlet and outlet molar flow rates. The term Wdenotes the weight of the catalyst used in the experiment (g), while ML corresponds to the metal loading, expressed as moles of metal per gram of catalyst. TOF_{ML} was used to compare catalysts prepared using different metal precursors, synthesis methods, and zeolite supports and allows direct comparison of different catalysts by referring the reaction rate to the amount of active metal species present.

Higher TOF_{ML} values were observed for copper nitrate–derived catalysts and for ZSM-5 zeolites, which was attributed to better metal dispersion.

The TOF value increases with increasing N_2O conversion until complete conversion is approached. At conversions close to 100 %, the TOF reaches an apparent maximum because the measured rate becomes limited by complete conversion rather than intrinsic kinetics. Under such conditions, further temperature increases do not lead to higher TOF values. A higher N_2O

feed concentration or flow rate can, however, result in larger TOF values by supplying more reactant to the active centers. As expected from the Arrhenius relationship, TOF increases at elevated temperatures. In contrast, when no N_2O conversion is observed, the TOF is zero.

4.1 Effect of Oxygen Concentration on Catalytic Performance in N_2O Decomposition

The influence of oxygen on the catalytic decomposition of $\boldsymbol{N_2O}$ was investigated under 10 vol% $\boldsymbol{O_2}$, corresponding to an oxygen flow of 20 mL/min in a total feed of 200 mL/min, with 1000 ppm $\boldsymbol{N_2O}$ balanced by helium. These reaction conditions were selected to simulate oxygen-rich exhaust environments encountered in ammonia combustion and nitric acid tail-gas processes. The catalytic performance of the Cu (Nitrate)-H-ZSM5-50-EIM catalyst prepared using 1.78 g of copper nitrate precursor was evaluated in terms of $\boldsymbol{N_2O}$ conversion, time-on-stream (TOS) stability, and intrinsic activity expressed as turnover frequency (TOF).

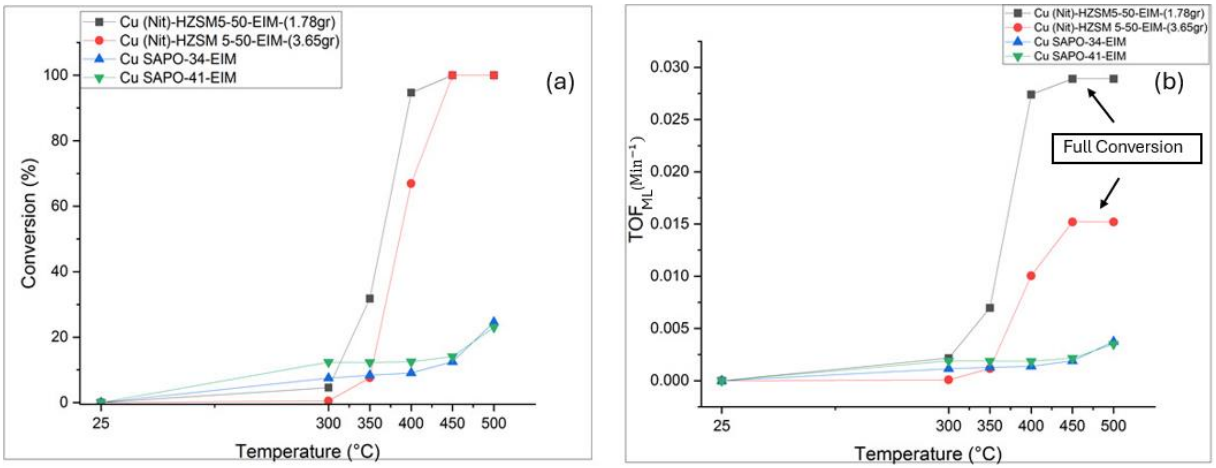

Figure 8: (a) N_2O conversion (%) Vs Temperature and (b) $\boldsymbol{TOF_{ML}(Min^{-1})}$ as a function of temperature for Cu-supported ZSM-5 SAPO-41, and SAPO-34 zeolite catalysts in the presence of 10 vol% $\boldsymbol{O_2}$.

Under oxygen-free conditions, all Cu-modified catalysts exhibited measurable activity toward N_2O decomposition. The $\boldsymbol{N_2O}$ conversion increased with temperature, and in some cases the temperature dependence became very steep, showing an exponential-like increase at higher temperatures. This activity is attributed to the presence of reduced or redox-active copper sites capable of activating the N–O bond, while differences in performance reflect variations in

copper dispersion, oxidation state distribution, and metal–support interactions. Catalysts based on SAPO frameworks generally showed superior low-temperature activity compared to conventional aluminosilicate zeolites, which can be linked to their distinct acidity and framework composition. In particular, the confinement effects of CHA- and AFO-type structures favor stabilization of isolated or binuclear Cu species that are highly active for N_2O dissociation.

The intrinsic catalytic behavior can be assessed from the TOF–temperature profiles if the $\boldsymbol{N_2O}$ conversion is below complete conversion. At low temperatures, TOF values are minimal, reflecting limited $\boldsymbol{N_2O}$ activation and extensive coverage of surface oxygen species. As the temperature increases, TOF rises due to enhanced N–O bond cleavage and partial regeneration of active sites. At higher temperatures, once the $\boldsymbol{N_2O}$ conversion approaches 100%, the apparent TOF tends to level off because the overall reaction rate becomes limited by the $\boldsymbol{N_2O}$ feed rather than by the intrinsic activity of the catalyst. In this regime, $\boldsymbol{N_2O}$ activation is no longer rate-limiting, and the removal of adsorbed oxygen species from the catalyst surface becomes the dominant rate-limiting step.

Upon introduction of oxygen into the feed, a systematic decrease in both $\boldsymbol{N_2O}$ conversion and TOF was observed for all catalysts, with the extent of inhibition increasing with $\boldsymbol{O_2}$ concentration. Under 10 vol% $\boldsymbol{O_2}$, TOF values are consistently lower than those obtained under oxygen-free conditions across the entire temperature range. This behavior indicates competitive adsorption and site blocking by oxygen-derived species and is consistent with the accepted mechanism of $\boldsymbol{N_2O}$ decomposition, in which surface oxygen recombination and desorption constitute the rate-determining step. At elevated oxygen partial pressures, accumulation of surface oxygen inhibits site regeneration, leading to partial deactivation.

Catalysts with higher copper dispersion and stronger metal–support interactions exhibit improved oxygen tolerance, suggesting that isolated or framework-stabilized Cu species are less susceptible to oxygen poisoning than aggregated CuO-like domains. Comparative analysis shows that SAPO-supported catalysts retain a larger fraction of their intrinsic activity under oxygen-rich conditions than ZSM-5 zeolite catalysts. This enhanced resistance is attributed to the lower framework aluminum content and better structural robustness of SAPO materials, which limit copper migration, suppress site blockage, and mitigate the intrinsic kinetic inhibition caused by excess oxygen.

Under oxygen-free conditions, the catalyst exhibits rapid activation with increasing temperature and achieves nearly complete $\boldsymbol{N_2O}$ conversion once the temperature exceeds approximately 400 °C. The conversion remains stable over extended time-on-stream, indicating efficient regeneration of active Cu sites in the absence of gas-phase oxygen. When oxygen is introduced into the reaction feed, a systematic decline in catalytic performance is observed. At 5 vol% $\boldsymbol{O_2}$, higher temperatures are required to reach comparable conversion levels, and a gradual decrease in conversion with TOS becomes evident, particularly at temperatures above 400 °C.

At 10 vol% $\boldsymbol{O_2}$, the inhibitory effect is significantly more pronounced. As shown in the conversion versus TOS profiles (Figure 9), $\boldsymbol{N_2O}$ conversion is almost the same as oxygen free conditions and with 5v% $\boldsymbol{O_2}$. Even at elevated temperatures where complete conversion is achieved at lower oxygen concentrations, the conversion has not decreased significantly and has the same stability as under 10 vol% $\boldsymbol{O_2}$. This trend clearly demonstrates that increasing oxygen concentration progressively slightly limits the availability of active sites for $\boldsymbol{N_2O}$ decomposition at lower temperatures such as under 400°C.

The observed inhibition can be rationalized based on the accepted reaction mechanism of $\boldsymbol{N_2O}$ decomposition over Cu-based zeolite catalysts. The reaction proceeds through adsorption of N_2O, cleavage of the N–O bond, and desorption of chemisorbed oxygen species. Among these steps, oxygen desorption is widely regarded as a rate-determining step. Under high oxygen partial pressure, such as 10 vol% $\boldsymbol{O_2}$, the catalyst surface becomes increasingly saturated with adsorbed oxygen species (O*), which hinders the regeneration of reduced Cu sites required for continuous catalytic turnover. As a result, both Langmuir–Hinshelwood recombination of adjacent oxygen species and Eley–Rideal pathways involving gas-phase $\boldsymbol{N_2O}$ are suppressed.

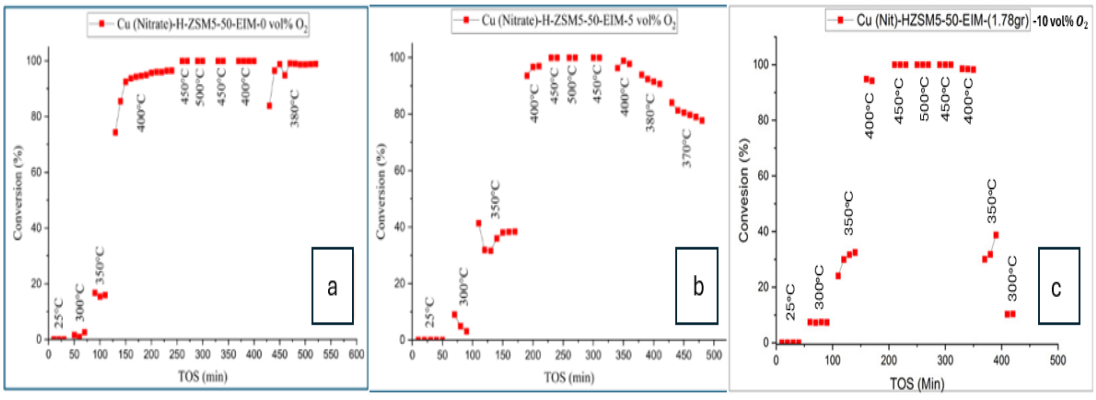

Figure 9: Catalytic conversion as a function of time on stream (TOS) for Cu nitrate–exchanged H-ZSM-5-50 catalysts prepared by EIM under stepwise temperature variation. (a) Cu (Nitrate)–H-ZSM-5-50-EIM operated

with 0 vol% O_2, (b) Cu (Nitrate)–H-ZSM-5-50-EIM operated with 5 vol% O_2 under an extended temperature program, and (c) Cu (Nitrate)–H-ZSM-5-50-EIM (1.78 g) operated with 10 vol% O_2. Reaction temperatures (25–500 °C) are indicated alongside the data points.

Characterization results support the conclusion that the observed deactivation under 10 vol% $\boldsymbol{O_2}$ is predominantly kinetic rather than structural. Nitrogen physisorption measurements showed only minor changes in surface area and micropore volume after the reaction, while SEM and XRD analyses confirm the preservation of the characteristic ZSM-5 crystal morphology and the absence of bulk CuO formation. Pyridine FTIR analysis reveals a high concentration of Lewis acid sites and a reduced Brønsted acidity for the Cu (Nitrate)-H-ZSM5-50-EIM zeolite catalyst, indicating that copper species are predominantly present as exchanged or highly dispersed Cu centers. Although these sites are catalytically active, they are particularly susceptible to oxygen saturation under oxygen-rich conditions.

4.2 Effect of Hydrothermal Stability under Steam-Containing Feeds

The hydrothermal stability of Cu-based zeolite catalysts is a key requirement for their application under realistic reaction conditions, where steam is inevitably present in the feed.

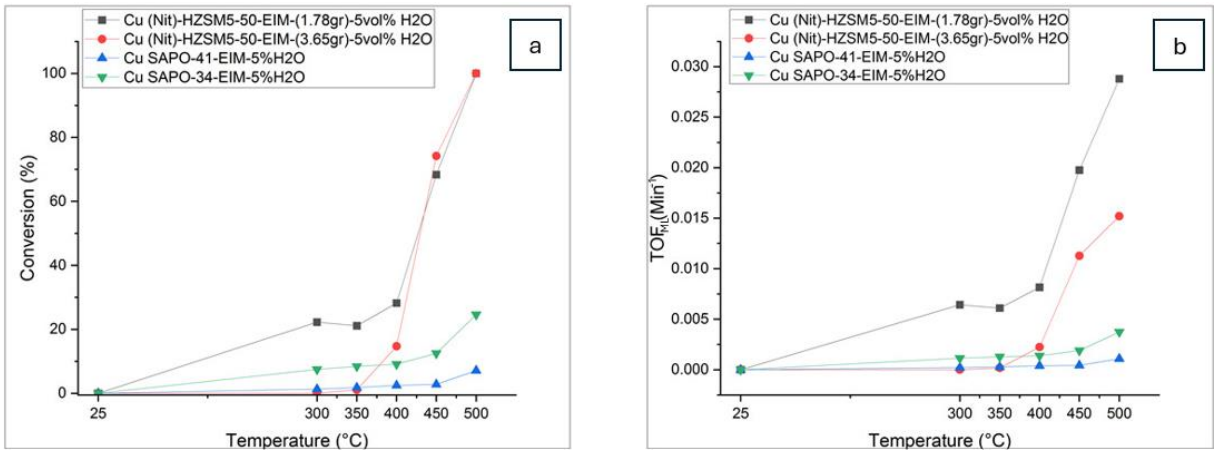

Figure 10: (a) N_2O conversion (%) and (b) turnover frequency (TOF, min^{-1}) as a function of reaction temperature over Cu (Nitrate)–HZSM-5-50-EIM catalysts with different copper loadings (1.78 g and 3.65 g) and Cu-supported SAPO-41 and SAPO-34 catalysts under 5 vol% H_2O. Reaction conditions: total flow rate of 200 mL min^{-1}, 1000 ppm N_2O balanced with He.

Figure 10 (a) presents the temperature-dependent N_2O conversion over Cu-modified HZSM-5, SAPO-41, and SAPO-34 catalysts under identical reaction conditions, while Figure 10 (b) shows the corresponding turnover frequency (TOF) profiles. A strong dependence of catalytic activity on catalyst composition, Cu nanoparticles size distributions, acidic properties and reaction temperature is evident.

Among all investigated catalysts, Cu (Nitrate)–HZSM-5-50-EIM (1.78 g) exhibited the highest and most consistent $\boldsymbol{N_2O}$ conversion across the studied temperature range. Negligible conversion was observed at low temperatures (≤300 °C) for all catalysts, indicating kinetic limitation associated with N–O bond activation. However, a sharp increase in N_2O conversion was observed for Cu/HZSM-5 zeolite-based catalysts above 350 °C.

At 400–500 °C, Cu (Nitrate)–HZSM-5-50-EIM (1.78 g) reached nearly complete conversion (~100%), outperforming the higher loading counterpart (3.65 g) as well as Cu-SAPO-41 and Cu-SAPO-34 catalysts. The superior performance at moderate-to-high temperatures suggests that this catalyst provides an optimal balance between accessible copper active sites and efficient oxygen removal from the surface, which is widely recognized as the rate-determining step in N_2O decomposition.

In contrast, Cu-SAPO-41 and Cu-SAPO-34 catalysts showed significantly lower conversions across the entire temperature range. Even at 500 °C, conversion over Cu-SAPO-34 remained below ~25%, while Cu-SAPO-41 exhibited only marginal improvement. This behavior can be attributed to differences in framework topology, location of Cu species, Cu nanoparticle size distributions, acidic properties and redox accessibility. The MFI structure of HZSM-5, with its intersecting medium-pore channels, is known to better stabilize isolated and binuclear Cu species, which are highly active for $\boldsymbol{N_2O}$ dissociation, compared to SAPO frameworks.

The intrinsic catalytic activity was further evaluated by analyzing the turnover frequency, as shown in Figure 10 (b). The TOF trends closely follow the conversion profiles but provide additional insight into the efficiency of the active sites.

Cu (Nitrate)–HZSM-5-50-EIM (1.78 g) displayed the highest TOF values at all temperatures above 350 °C, reaching approximately 0.03 min^{-1} at 500 °C, which is almost twice that of the higher-loading Cu/HZSM-5 catalyst and an order of magnitude higher than SAPO-based catalysts. This indicates that the enhanced activity is not merely due to a higher metal content

but rather to a higher fraction of catalytically effective copper sites. A similar trend was reported by Rahman, who observed that ZSM-5–based catalysts also achieved higher TOF values than other type of zeolite despite comparable or higher total copper loading, and attributed this behavior to better dispersion and stabilization of isolated and binuclear Cu species within the MFI framework. This consistency between the two studies confirms that optimal copper location and accessibility, rather than metal quantity alone, govern $\boldsymbol{N_2O}$ decomposition activity [56].

The lower TOF observed for the 3.65 g Cu/HZSM-5 catalyst suggests partial site crowding or the formation of less active copper species at higher loadings, which reduces the number of accessible redox-active Cu centers. For Cu-SAPO-41 and Cu-SAPO-34 zeolite catalysts, the consistently low TOF values confirm that only a small fraction of copper participates effectively in $\boldsymbol{N_2O}$ activation, likely due to stronger metal–framework interactions or diffusion limitations within smaller pore (0.58 nm) systems. Based on the combined evaluation of $\boldsymbol{N_2O}$ conversion and intrinsic activity (TOF), Cu (Nitrate)–HZSM-5-50-EIM (1.78 g) was selected as the optimal catalyst for detailed analysis in this thesis. Given its clearly superior catalytic performance, Cu (Nitrate)–HZSM-5-50-EIM (1.78 g) is discussed in detail in the subsequent sections of this thesis, including structure–activity relationships and stability considerations. The performance of the remaining catalysts, namely Cu (Nitrate)–HZSM-5-50-EIM (3.65 g), Cu-SAPO-41, and Cu-SAPO-34, is provided in Appendix B for completeness and comparative reference.

As shown in Figure 11, the hydrothermal stability of Cu (Nit)-HZSM5-50-EIM catalysts was evaluated under reaction conditions containing steam, using the catalyst operated with 10 vol% $\boldsymbol{O_2}$ in the feed as the reference system. This reference condition represents a non-steam oxidative environment and provides a baseline for assessing the impact of $\boldsymbol{H_2O}$ addition on catalytic performance, structure, and morphology.

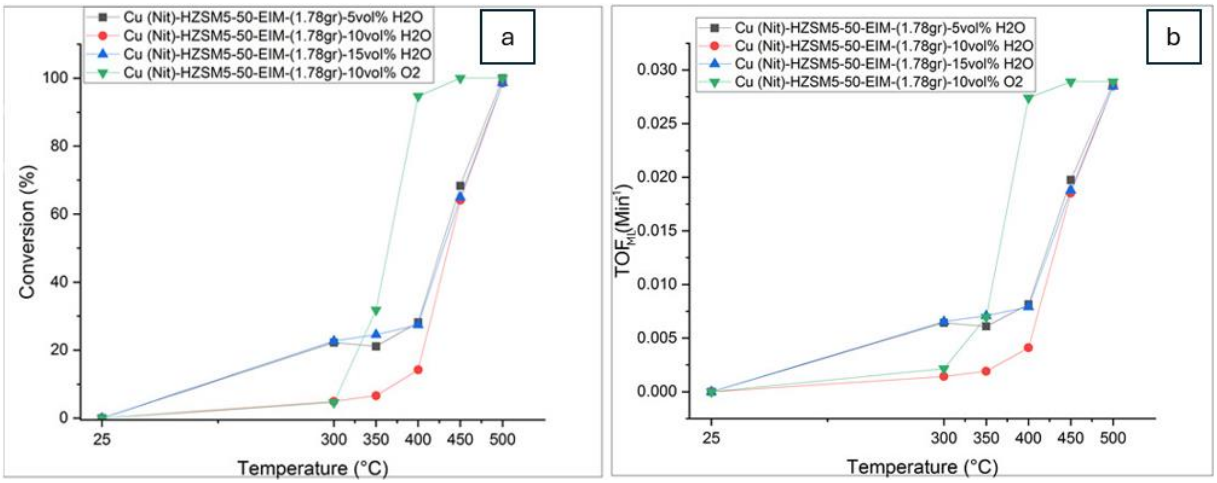

Figure 11: (a) N_2O conversion (%) and (b) turnover frequency (TOF, min^{-1}) as a function of reaction temperature over Cu (Nitrate)–HZSM-5-50-EIM (1.78 g) catalyst under different reaction atmospheres, including 5, 10, and 15 vol% H_2O and 10 vol% O_2. Reaction conditions: total flow rate of 200 mL min^{-1}, 1000 ppm N_2O balanced with He.

Under the reference conditions (10 vol% $\boldsymbol{O_2}$) the catalyst exhibits a steady increase in TOF with increasing temperature, reaching high activity at elevated temperatures due to efficient redox cycling of Cu species. Upon introducing steam into the feed, clear differences emerge. At temperatures below 300 °C, all catalysts display low TOF values, indicating kinetically limited behavior regardless of feed composition. However, at temperatures above 350 °C, catalysts operated with 5–10 vol% $\boldsymbol{H_2O}$ show TOF values comparable to or slightly higher than those observed under the 10 vol% $\boldsymbol{O_2}$ reference condition. This suggests that moderate steam levels do not deactivate the catalyst and may even promote activity by facilitating Cu redox transitions and maintaining active Cu sites.

In contrast, when the steam concentration is increased to 15 vol% $\boldsymbol{H_2O}$, the TOF enhancement becomes less pronounced relative to the $\boldsymbol{O_2}$ reference, particularly at higher temperatures. This behavior indicates the onset of mild hydrothermal effects, likely associated with partial dealumination, distortion of structures or redistribution of Cu species. Nevertheless, the catalyst retains substantial activity even under high steam content, demonstrating strong resistance to hydrothermal deactivation.

The influence of steam on the textural properties of the catalyst is summarized in Table(2) Relative to the 10 vol% $\boldsymbol{O_2}$ reference, Cu(Nit)-HZSM5-50-EIM samples exposed to 5–10 vol% H_2O maintain comparable surface areas (360–376 $m^2\ g^{-1}$) and micropore volumes (~0.14 cm^3

g^{-1}), indicating preservation of the microporous structure. At 15 vol% $\boldsymbol{H_2O}$, a significant reduction in the surface area and pore volume is observed; however, the median pore diameter remains nearly constant at approximately 0.58–0.59 nm, confirming that the HZSM-5 framework topology remains intact despite partial textural degradation.

Figure (12) presents the TEM micrographs and the corresponding particle size distribution profiles of the Cu (Nitrate)–HZSM-5-50-EIM (1.78 g) catalyst after $\boldsymbol{N_2O}$ decomposition in the presence of 10 vol% $\boldsymbol{O_2}$ with increasing water vapor concentrations. After the reaction with 10 vol% $\boldsymbol{O_2}$ without added $\boldsymbol{H_2O}$ (Figure a and a′), the catalyst preserves the characteristic crystalline morphology of the HZSM-5 framework, and copper species remain finely and homogeneously dispersed on the zeolite surface, with a relatively narrow particle size distribution centered around ~4–5 nm. This indicates that dry oxygen does not induce significant copper sintering and that the metal–support interaction remains strong. Upon addition of 5 vol% $\boldsymbol{H_2O}$ together with 10 vol% $\boldsymbol{O_2}$ (Figure b and b′), the copper particles remain well distributed, showing only a slight shift in the particle size distribution toward marginally smaller sizes (~3–4 nm) with limited broadening, suggesting that a low water content does not promote severe copper migration. When the water concentration is increased to 10 vol% (Figure c and c′), a modest increase in the average particle size (~5–6 nm) and a slightly broader distribution are observed; however, copper nanoparticles remain uniformly dispersed without formation of large agglomerates, and the zeolite framework remains intact. Even at the highest investigated water content of 15 vol% $\boldsymbol{H_2O}$ in the presence of 10 vol% $\boldsymbol{O_2}$ (Figure d and d′), the HZSM-5 framework retains its structural integrity, and the particle size distribution remains relatively close to those observed at lower water concentrations, with the mean particle sizes still within a narrow range (~6–7 nm). Importantly, no evidence of severe sintering or the framework collapse is observed, indicating good hydrothermal robustness of the Cu (Nitrate)–HZSM-5-50-EIM catalyst. Overall, the TEM results demonstrate that increasing water vapor concentration primarily induces a gradual and controlled redistribution of copper species rather than drastic particle growth or structural degradation, explaining why catalytic activity decreases moderately under high $\boldsymbol{H_2O}$ concentrations while the catalyst maintains structural stability and a significant fraction of accessible active sites. TEM imaging reveals that copper is well-dispersed throughout the zeolite crystal, with particles exhibiting a range of sizes. All observed particles are within the nanoscale, which may contribute to the enhanced catalytic activity of the material in $\boldsymbol{N_2O}$ decomposition.

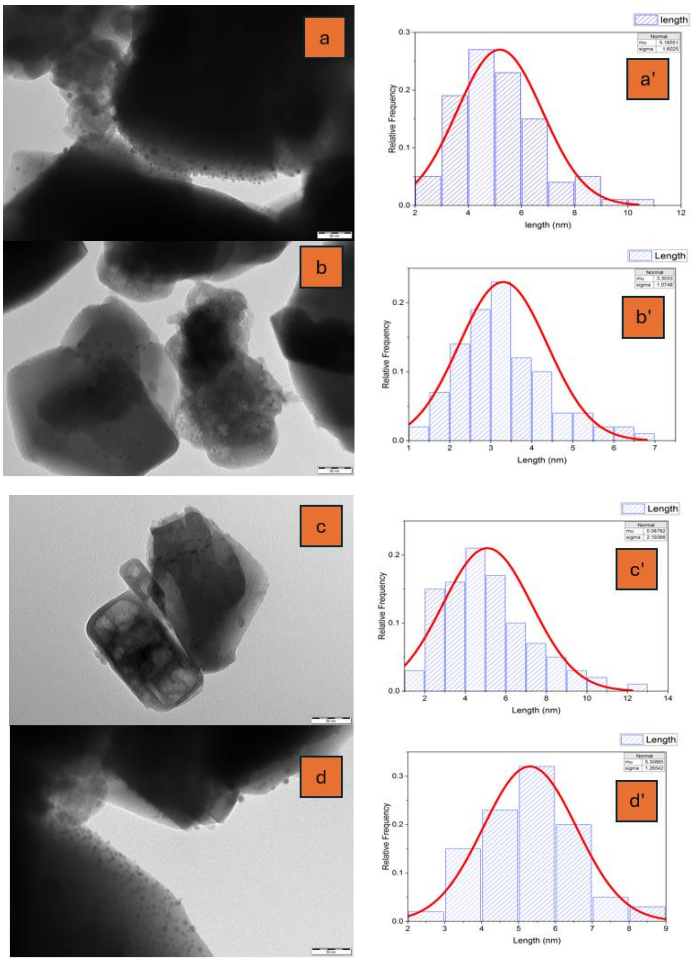

Figure 12: TEM images and corresponding copper particle size distribution histograms of the spent Cu (Nitrate)–HZSM-5-50-EIM (1.78 g) catalyst after $\boldsymbol{N_2O}$ decomposition under 10 vol% O_2 with increasing water vapor concentrations: (a, a′) after reaction with 10 vol% $\boldsymbol{O_2}$; (b, b′) after reaction with 5 vol% $\boldsymbol{H_2O}$ and 10 vol% $\boldsymbol{O_2}$; (c, c′) after reaction with 10 vol% $\boldsymbol{H_2O}$ and 10 vol% $\boldsymbol{O_2}$; and (d, d′) after reaction with 15 vol% $\boldsymbol{H_2O}$ and 10 vol% O_2. The histograms represent the particle size distributions of copper species fitted with normal distribution curves.

In addition, SEM micrographs demonstrate the excellent morphological stability of the catalyst under steam-containing reaction conditions. Relative to the 10 vol% $\boldsymbol{O_2}$ reference, catalysts exposed to up to 15 vol% $\boldsymbol{H_2O}$ retain intact particles with characteristic triangular and square crystal morphologies typical of the HZSM-5 framework. No particle breakage, surface cracking, or framework collapse is observed, confirming that the zeolite structure remains mechanically robust in the presence of steam.

Overall, Cu (Nit)-HZSM5-50-EIM exhibits high hydrothermal stability when compared to the 10 vol% $\boldsymbol{O_2}$ reference condition. Moderate steam concentrations (5–10 vol% $\boldsymbol{H_2O}$) maintain or slightly enhance catalytic activity while preserving structural and morphological integrity,

whereas higher steam levels induce only limited degradation. These results confirm the suitability of Cu (Nit)-HZSM-5-50-EIM catalyst for operation under realistic, steam-rich reaction environments.

5 Future Considerations

This research indicates that Cu-modified HZSM-5 shows encouraging activity and hydrothermal stability for $\boldsymbol{N_2O}$ decomposition; however, additional experimental studies are necessary to enhance catalyst performance and broaden its use in actual industrial settings. Future studies should embrace a more comprehensive strategy that combines catalyst composition, structure, reaction kinetics, and durability over time.

An essential focus for upcoming research is the methodical assessment of copper loading on zeolite-derived catalysts. This thesis highlights more efficient Cu loading for Cu–HZSM-5 by evaporation impregnation; however, investigating a wider spectrum of metal concentrations on HZSM-5 and SAPO-based catalysts could yield better understanding of the interplay between copper dispersion, active site density, and oxygen elimination kinetics. These studies may elucidate the shift from isolated Cu species, typically more active, to aggregated copper phases that could adversely affect intrinsic activity and hydrothermal stability.

Simultaneously, broadening the variety of zeolite framework structures is crucial for discovery of highly efficient and hydrothermally stable transition metal modified catalysts for N_2O decomposition. Alternative frameworks exhibiting enhanced hydrothermal stability and redox capabilities, like SSZ-13 and SSZ-39 featuring CHA topology, have demonstrated remarkable durability against steam-induced dealumination in relevant nitrogen conversion processes. Exploring Cu-exchanged SSZ-type zeolites for $\boldsymbol{N_2O}$ decomposition might clarify the impact of pore structure, framework makeup, and confinement effects on oxygen inhibition, copper speciation, and catalyst longevity.

In addition to catalyst composition, future research should concentrate on the direct detection of active copper species during reaction conditions. Although ex situ characterization provides important structural details, the oxidation state and coordination environment of copper during $\boldsymbol{N_2O}$ decomposition—particularly when oxygen and steam are present—are quite variable. Consequently, methods capable of probing catalysts under relevant conditions are needed. While X-ray absorption techniques such as XANES/EXAFS are frequently applied ex situ or quasi in situ, their operando implementation remains challenging. Complementary in situ or operando methods, including DRIFTS and UV–Vis spectroscopy, could enable real-time

monitoring of Cu^{+}/Cu^{2+} interconversion and help correlate catalytic performance with changes in active sites.

Additional mechanistic understanding may be gained by focusing on the kinetics of oxygen removal, recognized as a crucial rate-limiting factor. Transient experiments, such as oxygen pulsing, isotopic labeling with $^{18}O_2$ or $N_2{}^{18}O$, and temperature-programmed surface reaction (TPSR) analyses, may assist in differentiating between Langmuir–Hinshelwood and Eley–Rideal mechanisms and measuring oxygen mobility in various zeolite structures.

The impact of catalyst structure, oxidation states of metals and diffusion constraints also require additional exploration. While intrinsic activity was evaluated via turnover frequency, internal mass transfer effects could still influence results, especially for catalysts featuring narrow pore structures like SAPO-34 and SAPO-41. Creating catalysts with regulated crystal dimensions or hierarchical porosity and assessing their performance at different space velocities would aid in separating diffusion effects from fundamental kinetics.

Moreover, future efforts need to expand the variety of reaction conditions studied to more accurately reflect industrial settings. Variables like space velocity, $\boldsymbol{N_2O}$ inlet concentration, total pressure, and temperature fluctuations need to be altered systematically. The influence of common exhaust gas constituents, such as NO, $\boldsymbol{NO_2}$, and leftover $\boldsymbol{NH_3}$, must also be examined to evaluate catalyst selectivity, poisoning resistance, and operational durability.

Ultimately, more focus needs to be directed toward catalyst regeneration, reuse and enduring stability. Examining the reversibility of deactivation caused by oxygen and steam via repeated reaction-regeneration cycles, managed redox treatments, and prolonged time-on-stream tests would offer vital understanding of catalyst durability and degradation processes. Extended steady-state tests, especially, would better mirror industrial operation and uncover gradual structural or chemical alterations that might not be apparent in short-term trials.

6 Conclusion

This thesis explored the direct catalytic breakdown of nitrous oxide ($\boldsymbol{N_2O}$) using copper-modified zeolite catalysts, focusing specifically on the impact of oxygen levels and hydrothermal stability in industrially relevant situations. Cu-modified HZSM-5, SAPO-34, and SAPO-41 zeolite catalysts were prepared via evaporation impregnation and thoroughly assessed using comprehensive physicochemical characterization and catalytic performance tests in $\boldsymbol{N_2O}$ decomposition reaction.

Of the analyzed catalysts, Cu (Nitrate)–HZSM-5-50 with a moderate copper load exhibited the highest catalytic performance and inherent turnover frequency for N_2O decomposition. The excellent performance of this catalyst is due to the efficient distribution of redox-active copper species inside the MFI framework, which aids in N–O bond activation and enhances effective catalytic cycling. In comparison, Cu-supported SAPO-34 and SAPO-41 catalysts demonstrated much lower activity, probably due to variations in framework topology, copper positioning, and restricted access to active sites.

The effect of oxygen concentration was primarily kinetic rather than structural. Raising oxygen partial pressure led to a detectable decrease $\boldsymbol{N_2O}$ conversion and TOF, aligning with competitive adsorption and the build-up of surface oxygen species that obstruct active site regeneration. Nonetheless, the structural analysis of used catalysts demonstrated that the zeolite framework and copper distribution were mostly maintained, suggesting that oxygen-driven deactivation primarily happens via reversible site blocking instead of irreversible catalyst deterioration.

Hydrothermal stability evaluations indicated that the Cu (Nitrate)–HZSM-5-50 catalyst shows significant resilience against deactivation caused by steam. Moderate concentrations of water vapor (5–10 vol%) did not substantially hinder catalytic performance and, in some instances, slightly improved activity, potentially by promoting copper redox cycling. Despite the increased steam content (15 vol%), only minor textural deterioration and moderate copper redistribution were noted, while the zeolite structure and catalytic performance in N_2O decomposition remained mostly preserved. These findings validate the stability of Cu–HZSM-5 in genuine exhaust gas environments.

This research shows that Cu-modified HZSM-5 is an exceptionally effective catalyst for the direct breakdown of $\boldsymbol{N_2O}$, featuring significant inherent activity along with robust resistance to oxygen inhibition and hydrothermal aging. The results offer important understanding of structure–activity–stability connections and aid in the systematic development of long-lasting, non-noble metal catalysts for industrial $\boldsymbol{N_2O}$ decomposition.

7 References:

1. **Zhuang, Y., Li, P., & Xu, H.** (2024). Mechanistic insights into nitrous oxide decomposition over transition metal catalysts: A review. *Chemical Engineering Journal, 475*, 146239. https://doi.org/10.1016/j.cej.2024.146239
2. **Konsolakis, M.** (2015). Recent advances on nitrous oxide (N_2O) decomposition over non-noble metal oxide catalysts: Catalytic performance, mechanistic considerations, and surface chemistry aspects. *ACS Catalysis, 5*(2), 639–663. https://doi.org/10.1021/cs5014042
3. **Wu, Y., Zhang, L., & Li, H.** (2024). Nitrous oxide: Trends, sources, and mitigation. *Chemical Society Reviews, 53*(3), 1256–1287. https://doi.org/10.1039/d3cs00984g
4. **Palella, A., Arena, F., & Parmaliana, A.** (2003). Comparative study of hydrothermal stability of Cu–ZSM-5 and CuAPSO-34 catalysts for N_2O decomposition. *Journal of Catalysis, 215*(1), 1–9. https://doi.org/10.1016/S0021-9517(02)00023-1
5. **Palella, A., Arena, F., & Parmaliana, A.** (2006). Rare-earth promotion of Cu–ZSM-5 for nitrous oxide decomposition in steam-containing atmospheres. *Kinetics and Catalysis, 47*(2), 258–264. https://doi.org/10.1134/S0023158406020151
6. **Farhan, M., Ahmed, S., Al-Otaibi, R., & Khan, A.** (2022). Density functional theory and QM/MM study on dicopper active sites for nitrous oxide decomposition: Inhibitory effect of water. *Catalysis Science & Technology, 12*(4), 1150–1163. https://doi.org/10.1039/d1cy01954j
7. **Zhang, W., Liu, Y., & Chen, G.** (2023). Hydrothermal deactivation of Ru and Rh catalysts during nitrous oxide decomposition. *Catalysis Today, 404*, 32–42. https://doi.org/10.1016/j.cattod.2022.05.011
8. **Satsuma, A., Hattori, T., & Tanaka, T.** (2001). Decomposition of nitrous oxide over cobalt oxide catalysts. *Applied Catalysis B: Environmental, 29*(2), 103–113. https://doi.org/10.1016/S0926-3373(00)00193-1
9. **Yang, F., Liu, X., & Zhao, J.** (2025). Stability of transition metal catalysts for nitrous oxide decomposition under hydrothermal conditions. *Chemical Engineering Science, 280*, 118734. https://doi.org/10.1016/j.ces.2024.118734
10. **Kögel, M., Richter, M., Eckelt, R., & Parlitz, B.** (1998). Rare earth modification of Cu–ZSM-5 for enhanced hydrothermal stability. *Journal of Molecular Catalysis A: Chemical, 136*(2–3), 213–224. https://doi.org/10.1016/S1381-1169(98)00115-2
11. **Yang, H., Zhao, Q., & Sun, C.** (2020). Post-synthetic modification of zeolites to improve hydrothermal stability of Cu–ZSM-5 for N_2O decomposition. *Microporous and Mesoporous Materials, 302*, 110246. https://doi.org/10.1016/j.micromeso.2020.110246
12. **Shih, Y. C., Kots, P., & Buda, C.** (2020). Active site dynamics in Cu-zeolites for N_2O decomposition and side reactions in NH_3-SCR. *Journal of Catalysis, 389*, 42–55. https://doi.org/10.1016/j.jcat.2020.05.002
13. **Tang, X., Chen, W., & Wang, Y.** (2022). Oxygen vacancies and Co^{3+}/Co^{2+} redox pairs in Co-based oxides for N_2O decomposition. *Journal of Environmental Chemical Engineering, 10*(5), 108345. https://doi.org/10.1016/j.jece.2022.108345
14. **Zabilskiy, M., Djinović, P., & Pintar, A.** (2017). Synergistic redox activity in Cu/CeO_2 catalysts for nitrous oxide decomposition. *Journal of Catalysis, 345*, 157–167. https://doi.org/10.1016/j.jcat.2016.11.009
15. **Maitarad, P., Limtrakul, J., & Illas, F.** (2015). Decomposition of nitrous oxide on transition metal porphyrins: A density functional theory study. *Physical Chemistry Chemical Physics, 17*(4), 2904–2914. https://doi.org/10.1039/c4cp04562e

16. **Yun, C., Kim, J., & Lee, S.** (2021). Effect of oxygen concentration on nitrous oxide decomposition over Cu-zeolites. *ACS Omega, 6*(3), 1785–1794. https://doi.org/10.1021/acsomega.0c05463
17. **Xia, Y., Zhou, H., & Chen, J.** (2019). Inhibitory effects of water vapor on N_2O decomposition over Cu-exchanged zeolites. *Catalysis Today, 327*, 177–185. https://doi.org/10.1016/j.cattod.2018.07.036
18. **Grzybek, T., Samojeden, B., & Legutko, P.** (2022). The role of NOx in nitrous oxide decomposition over transition metal catalysts. *Applied Catalysis B: Environmental, 318*, 121755. https://doi.org/10.1016/j.apcatb.2022.121755
19. **Kim, H., Jang, E., Jeong, Y., Kim, J., Kang, C. Y., Kim, C. H., Baik, H., Lee, K. Y., & Choi, J.** (2018). On the synthesis of a hierarchically structured ZSM-5 zeolite and the effect of its physicochemical properties with Cu impregnation on cold-start hydrocarbon trap performance. *Catalysis Today*, *314*, 78–93. https://doi.org/10.1016/j.cattod.2018.02.008
20. **Palella, A., Arena, F., & Parmaliana, A.** (2003). Comparative study of hydrothermal stability of Cu–ZSM-5 and CuAPSO-34 catalysts for N_2O decomposition**.** *Journal of Catalysis, 215(1), 1–9.* https://doi.org/10.1016/S0021-9517(02)00023-1
21. **Bartholomew, C. H., & Farrauto, R. J.** (2006). Fundamentals of industrial catalytic processes (2nd ed.). *Wiley.*
22. **Yang, F., Liu, X., & Zhao, J.** (2025). Stability of transition metal catalysts for nitrous oxide decomposition under hydrothermal conditions. *Chemical Engineering Science*, 280**,** 118734. https://doi.org/10.1016/j.ces.2024.118734
23. **Shih, Y. C., Kots, P., & Buda, C.** (2020). Active site dynamics in Cu-zeolites for N_2O decomposition and side reactions in NH_3-SCR. *Journal of Catalysis 389,* 42–55. https://doi.org/10.1016/j.jcat.2020.05.002
24. **Yun, C., Kim, J., & Lee, S.** (2021). Effect of oxygen concentration on nitrous oxide decomposition over Cu-zeolites. *ACS Omega, 6(3),* 1785–1794. https://doi.org/10.1021/acsomega.0c05463
25. **Xia, Y., Zhou, H., & Chen, J.** (2019). Inhibitory effects of water vapour on N_2O decomposition over Cu-exchanged zeolites. *Catalysis Today, 327,* 177–185. https://doi.org/10.1016/j.cattod.2018.07.036
26. **Storck, S., Bretinger, H., & Maier, W. F.** (1998). Characterization of micro- and mesoporous solids by physisorption methods and pore-size analysis. *Applied Catalysis A: General, 174*(1–2), 137–146.
27. ***Leofanti, G., Padovan, M., Tozzola, G. & Venturelli, B****. (1998).* Surface area and pore texture of catalysts. *Catalysis Today 41, 207–219.*
28. **Zhang, S. & Wang, C**. (2023). Precise Analysis of Nanoparticle Size Distribution in TEM Image. Methods Protoc. 6, 63.
29. **Emeis, C. A.** (1993). Determination of Integrated Molar Extinction Coefficients for Infrared Absorption Bands of Pyridine Adsorbed on Solid Acid Catalysts. *Catalysis Today 141*, 347–354.
30. **Gauli, B.** (2021). Hydrodeoxygenation of lignin-derived model compound isoeugenol over Fe-, Ni-, and Fe–Ni-supported on zeolites.
31. **Zou, W., Zhang, J., Wang, W., Li, H., Jiang, L., & Liu, H.** (2014). Catalytic decomposition of N_2O over Cu-ZSM-5 nanosheets. *Journal of Molecular Catalysis A: Chemical, 394*, 83–88.
32. **Cullity, B. D., & Stock, S. R.** (2014). Elements of X-ray Diffraction (3rd ed.). Boston, MA: Pearson Education.
33. **Rigaku Corporation.** (2015). D/MAX 2500 X-ray Diffractometer Instruction Manual. Tokyo, Japan: Rigaku Corporation.

34. **Shih, A. J., González, J. M., Khurana, I., Pérez Ramírez, L., Peña, A., Kumar, A., & Villa, A. L.** (2021). *ACS Catalysis, 11*(16), 10362–10376.

35. **Janssens, T. V. W., Falsig, H., Lundegaard, L. F., Vennestrøm, P. N. R., Rasmussen, S. B., Moses, P. G., Giordanino, F., Borfecchia, E., Lomachenko, K. A., Lamberti, C., Bordiga, S., Godiksen, A., Mossin, S., & Beato, P.** (2015). *A* consistent reaction scheme for the selective catalytic reduction of nitrogen oxides with ammonia. *ACS Catalysis, 5(5),* 2832–2845.

36. **Yu, J. & Li, Y**. (2014). New stories of zeolite structures: their descriptions and predictions. *Chemical Reviews, 114(14), 7268–7316.*

37. **Védrine, J.C**. (2014). Revisiting active sites in heterogeneous catalysis. *Applied Catalysis A: General, 481*, 217–232.

38. **Armandi, M., et al.** (2019). Effect of preparation technique on Cu-ZSM-5 oscillatory behaviour. *Catalysis Today*.

39. ***Lok, B. M., Messina, C. A., Patton, R. L., Gajek, R. T., Cannan, T. R., & Flanigen, E. M.*** *(1982).* Crystalline silicoaluminophosphates. *Union Carbide Corporation. U.S. Patent No. 4,310,440.*

40. **Mertens, M. M., & Verberckmoes, A.** (2005). Synthesis of silicoaluminophosphate molecular sieves. *In Synthesis of Molecular Sieves* (123–148).

41. **Mériaudeau, P., Tuan, V. A., Lefebvre, F., Nghiem, V. T., & Naccache, C.** *(1998).* Synthesis and characterization of SAPO-41: Effect of the silicon content and the crystal size on the hydroisomerization of n-octane over Pt–Pd/SAPO-41. *Microporous and Mesoporous Materials, 26*, 161–173.

42. **Ertl, G., Knözinger, H., Schüth, F., & Weitkamp, J. (Eds.).** *(2008).* Handbook of heterogeneous catalysis (Vol. 1, pp. 484–510). *Wiley-VCH.*

43. **Din, I. U., Nasir, Q., Garba, M. D., Alharthi, A. I., Alotaibi, M. A., & Usman, M.** (2022). A review of preparation methods for heterogeneous catalysts. *Mini-Reviews in Organic Chemistry, 19*(1), 92-110

44. **Brunauer, S., Emmett, P. H., & Teller, E.** (1938). Adsorption of gases in multimolecular layers. *Journal of the American Chemical Society, 60*(2), 309–319.

45. **Dubinin, M. M.** (1967). Adsorption in micropores. *Journal of Colloid and Interface Science, 23*(4), 487–499.

46. **Terasaki, O., & Ohsuna, T.** (1995). What can we observe in zeolite related materials by HRTEM? *Catalysis Today, 23*(2–3), 201–218.

47. **Souza, M. J. B., Araujo, A. S., Pedrosa, A. M. G., Marinkovic, B. A., Jardim, P. M., & Morgado Jr., E.** (2006). Textural features of highly ordered Al-MCM-41 molecular sieve studied by X-ray diffraction, nitrogen adsorption and transmission electron microscopy. *Materials Letters, 60*(23), 2682–2685.

48. **Pirola, C., Galli, F., & Patience, G. S.** (2018). Experimental methods in chemical engineering: Temperature programmed reduction—TPR. *Chemical Engineering, 96,* 2317–2320.

49. **Villarroel-Rocha, J., & Gil, A**. (2024). Modeling the temperature-programmed reduction of metal oxide catalysts by considering the particle-size distribution effect. *Chemical Engineering Journal, 487*, 150722.

50. **Heidebrecht, P., Galvita, V., & Sundmacher, K.** (2008). An alternative method for parameter identification from temperature programmed reduction (TPR) data. *Chemical Engineering Science, 63,* 4776–4788.

51. **Khan, H., Yerramilli, A. S., D'Oliveira, A., Alford, T. L., Boffito, D. C., & Patience, G. S.** (2020). Experimental methods in chemical engineering: X-ray diffraction spectroscopy—XRD. *Chemical Engineering, 98*(6), 1255–1266. https://doi.org/10.1002/cjce.23747

52. **Haber, J., Block, J. H., & Delmon, B.** (1995). Manual of methods and procedures for catalyst characterization (Technical Report). *Pure and Applied Chemistry,* 67(8–9), 1257–1306. https://doi.org/10.1351/pac199567081257
53. **Gallego-Villada, L. A., Perez-Sena, W. Y., Sánchez-Velandia, J. E., Cueto, J., Alonso-Doncel, M. del M., Wärnå, J., Mäki-Arvela, P., Alarcón, E. A., Serrano, D. P., & Murzin, D. Y.** (2024). Dendritic ZSM-5 zeolites as highly active catalysts for the valorization of monoterpene epoxides. *Green Chemistry, 26*, 10512–10528.
54. **Gallego-Villada, L. A., Alarcón, E. A., & Villa, A. L.** (2021). Effect of Colombian raw materials on the Prins condensation reaction over Sn/MCM-41. *Catalysis Today, 372*, 36–50.
55. Database of Zeolite Structures. https://www.iza-structure.org/databases/.
56. **Rahman, M. H.** (2025). Direct catalytic decomposition of N_2O over Cu- and Fe-modified Beta, USY, and ZSM-5 zeolite catalysts

8 Appendix A

8.1 Flow calibration

For calibration of the feed gas flow rates, an Agilent Technologies Opti-Flow 650 digital flow meter was used to measure the high flow rates of helium carrier gas, while a Hamonic 520 digital flow meter was employed for the low flow rates of N_2O. Calibration was performed over a range of valve openings, and the corresponding flow rates were recorded systematically. Based on the collected data, calibration equations were subsequently derived.

8.1.1 Helium flow rate calibration

Table 8.1: Helium flow-rate calibration at 5.5bar, 296.15K at different % of maximum flow.

0	16.1	30.4	44.40	73.2	88.3	102	117	132	142	173	201	228	260	290
0	16.2	30.1	44.40	74.2	88.2	104	117	131	143	172	200	230	263	288
0	16.3	30.1	44.10	73.1	88.1	103	118	127	141	171	200	230	263	289
0	16.2	30	44.30	73.3	88.4	102	116	128	143	171	201	230	262	290
0	16.2	30.3	44.10	73.5	88.2	104	117	132	143	174	202	230	262	289
0	16.1	30	44.20	73.6	88.4	105	116	131	-	173	200	230	263	-
0	16.2	29.8	44.20	73.3	88.2	103	117	130	-	-	-	-	-	-
0	-	29.6	44.20	73.1	-	103	117	132	-	-	-	-	-	-
0	-	29.7	-	73	-	103	118	133	-	-	-	-	-	-
0	-	29.6	-	-	-	101	117	131	-	-	-	-	-	-
0	-	29.7	-	-	-	102	-	133	-	-	-	-	-	-
0	-	29.5	-	-	-	103	-	133	-	-	-	-	-	-
0	-	29.4	-	-	-	-	-	131	-	-	-	-	-	-
0	-	29.3	-	-	-	-	-	132	-	-	-	-	-	-
0	-	29.3	-	-	-	-	-	-	-	-	-	-	-	-
Avg,0	16.2	29.8	44.24	73.5	88.26	103.2	117	131.1	142.4	172.3	201	229.7	262	289

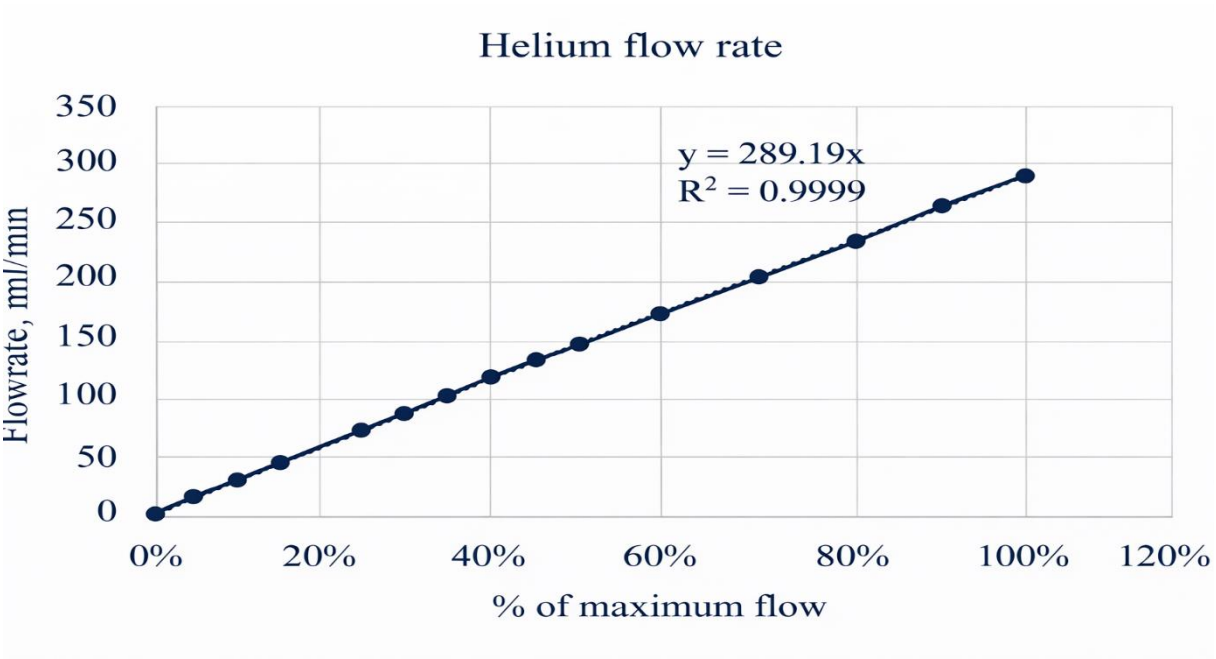

Figure 8.1: Linear relationship between helium flow rate (mL/min) and percentage of maximum flow, demonstrating excellent proportionality across the operating range (y = 289.19x, R² = 0.9999).

8.1.2 Nitrous oxide flow rate calibration

Table 8.2: N_2O flow rate at 1bar & 296.15K at different % of maximum flow.

0%	15%	20%	25%	50%	75%
0	0.63	0.93	1.14	2.23	3.31
0	0.63	0.91	1.12	2.27	3.23
0	-	0.95	1.14	2.24	3.21
0	-	0.96	-	2.24	3.31
0	-	-	-	2.25	3.33
0	-	-	-	2.24	3.28
0	-	-	-	2.27	3.41
0	-	-	-	-	3.51
0	-	-	-	-	3.35
0	-	-	-	-	3.21
0	-	-	-	-	3.44
Average, 0	0.63	0.9375	1.13	2.24	3.32

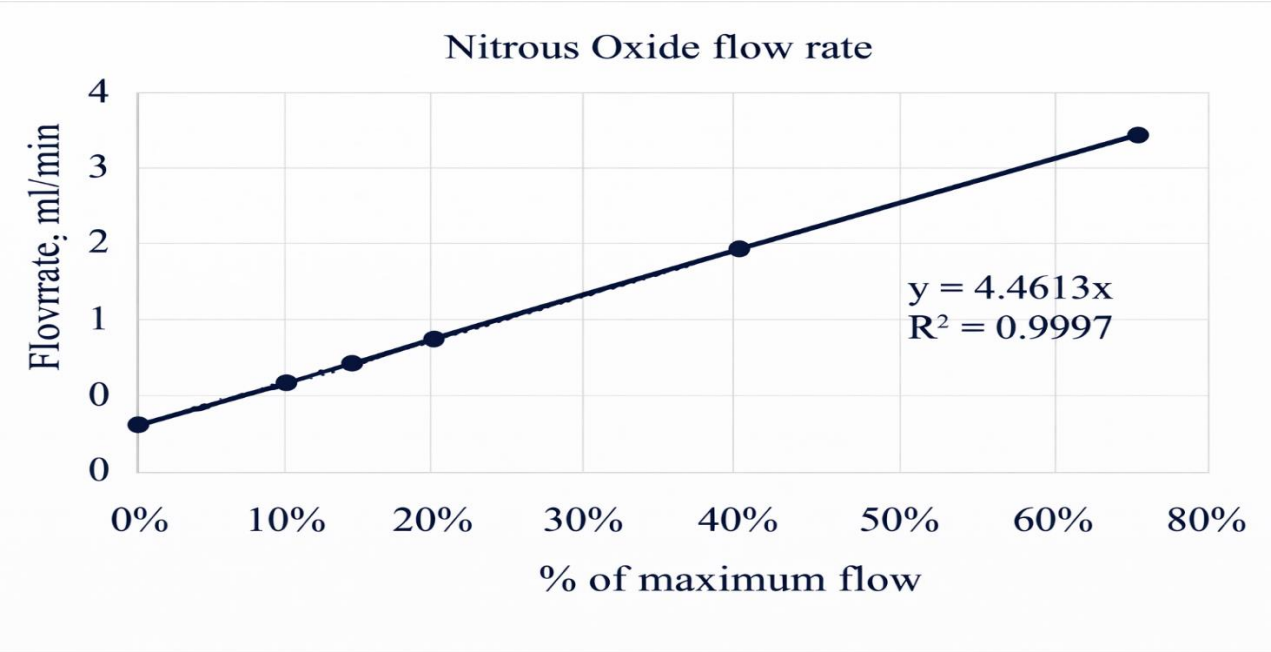

Figure 8.2: N_2O flow rates at 1 bar & 296.15K at different % of maximum flow

8.1.3 Oxygen flow rate calibration

Table 8.3: O_2 flow rate calibration at 1.1 bar, 296.15K at different valve openings.

Measurement	**0%**	**15%**	**20%**	**25%**	**30%**	**40%**
Trial 1	0	4.52	5.95	7.56	8.74	11.5
Trial 2	0	4.47	5.96	7.58	8.77	11.6
Trial 3	0	4.50	5.89	7.52	8.70	11.5
Trial 4	0	4.54	5.97	—	8.74	11.6
Trial 5	0	—	5.93	—	8.79	11.6
Trial 6	0	—	—	—	—	11.7
Trial 7	0	—	—	—	—	11.5
Average	**0**	**4.50**	**5.94**	**7.55**	**8.74**	**11.57**

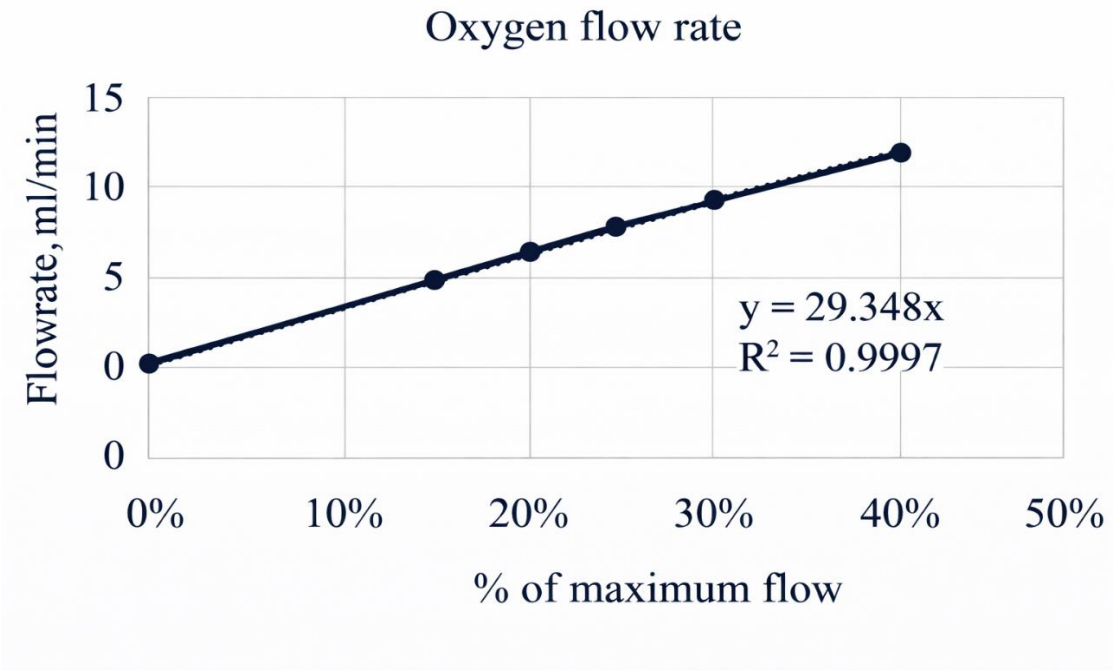

Figure 8.3: O_2 flow rate calibration at 1.1 bar, 296.15K at different valve openings.

8.1.4 GC Calibration

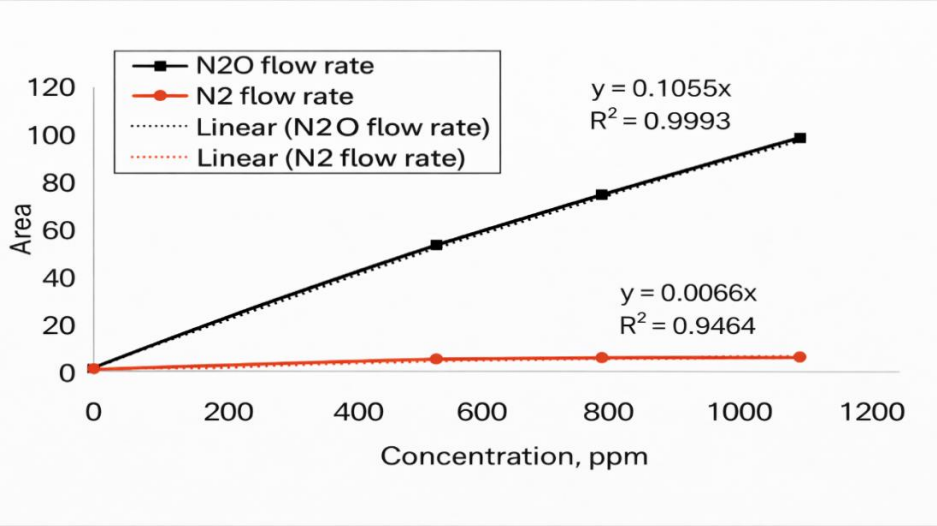

Figure 8.4: GC calibration for nitrous oxide & nitrogen in an empty reactor at 24ºC.

9 Appendix B

9.1 Experimental Results

9.1.1 Effect of Water Concentration on the Time-on-Stream Performance of Cu SAPO-41 zeolite catalyst

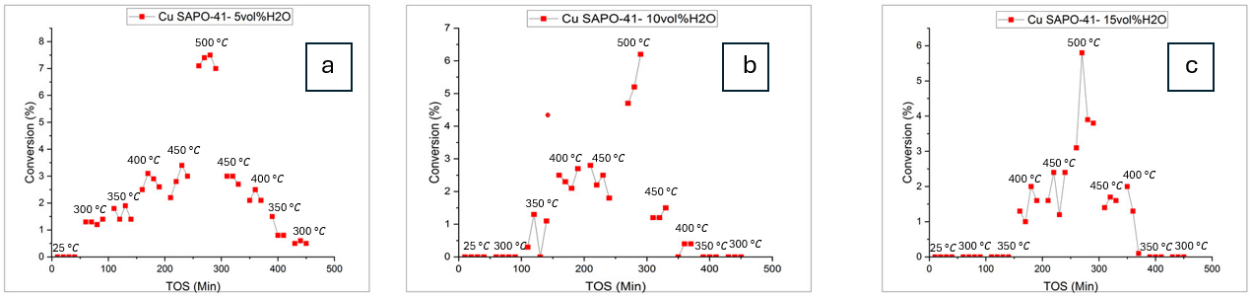

Figure 9.1: Conversion (%) as a function of time-on-stream (TOS) for Cu SAPO-41-EIM under different water concentrations in the feed: (a) 5 vol% H_2O, (b) 10 vol% H_2O, and (c) 15 vol% H_2O, showing the effect of water content on catalytic activity and stability.

Figure (9.1) shows the time-on-stream performance of Cu SAPO-41-EIM with different water concentrations of 5, 10, and 15 vol% H_2O. At 5 vol% H_2O, the catalyst displayed the highest and most consistent activity, with conversion steadily rising from almost zero to about 7–7.5% after approximately 260–280 min at 500°C on stream, then experiencing a gradual decrease at extended TOS. As the water concentration rose to 10 vol% H_2O, the highest conversion fell to approximately 6–6.5% at 500°C, and the catalyst became inactive more quickly, with conversion reaching nearly zero after around 350 minutes. At 15 vol% H_2O, Cu SAPO-41-EIM exhibited the least stability, demonstrating a brief peak conversion of approximately 5.5–6% at 500°C before quickly deactivating. The findings suggest that although a small quantity of water can enhance catalyst activation, increased water levels negatively impact both activity and stability.

9.1.2 Effect of Water Concentration on the Time-on-Stream Performance of Cu SAPO-34 zeolite catalyst

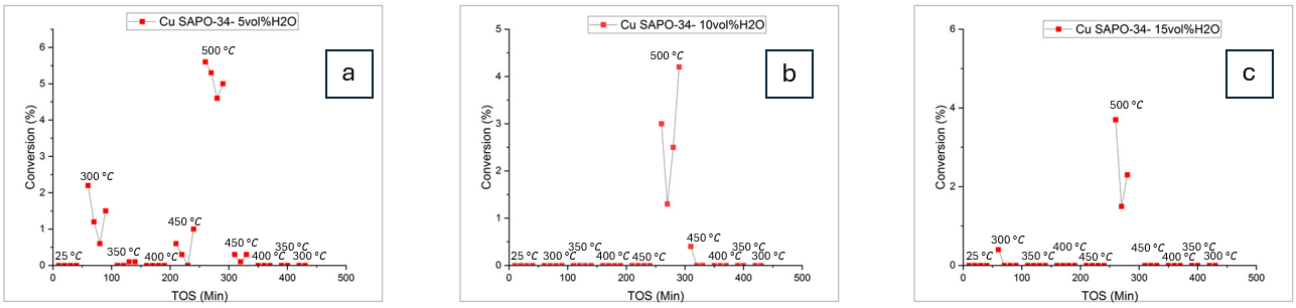

Figure 9.2: Conversion (%) as a function of time-on-stream (TOS) for Cu SAPO-34-EIM under different water concentrations in the feed: (a) 5 vol% H_2O, (b) 10 vol% H_2O, and (c) 15 vol% H_2O, showing the effect of water content on catalytic activity and stability.

Figure (9.2) depicts the catalytic performance of Cu SAPO-34-EIM under wet conditions (5–15 vol% H_2O) based on temperature and as a function of time-on-stream. At every water

concentration, minimal conversion occurs at low temperatures (25–300 °C), which suggests the catalyst is not sufficiently activated. With rising temperature, a significant enhancement in activity is noted, peaking consistently at 500 °C. At 5 vol% H_2O, Cu SAPO-34 achieves a peak conversion of about 5–5.5% at 500 °C, whereas only minor and inconsistent activity is observed at 350–450 °C. Raising the water concentration to 10 vol% H_2O results in a lower peak conversion of ~4–4.5% at 500 °C, along with faster deactivation. At 15 vol% H_2O, the catalyst displays the least activity, reaching a peak conversion of approximately 3–4% at 500 °C and nearly zero conversion at lower temperatures. These findings indicate that elevated reaction temperature is crucial for activating Cu SAPO-34-EIM in moist conditions; however, a rise in water concentration markedly hinders catalytic efficiency and stability, probably due to the competitive adsorption of water and intensified hydrothermal impacts that restrict the availability and longevity of Cu active sites in the SAPO-34 structure.

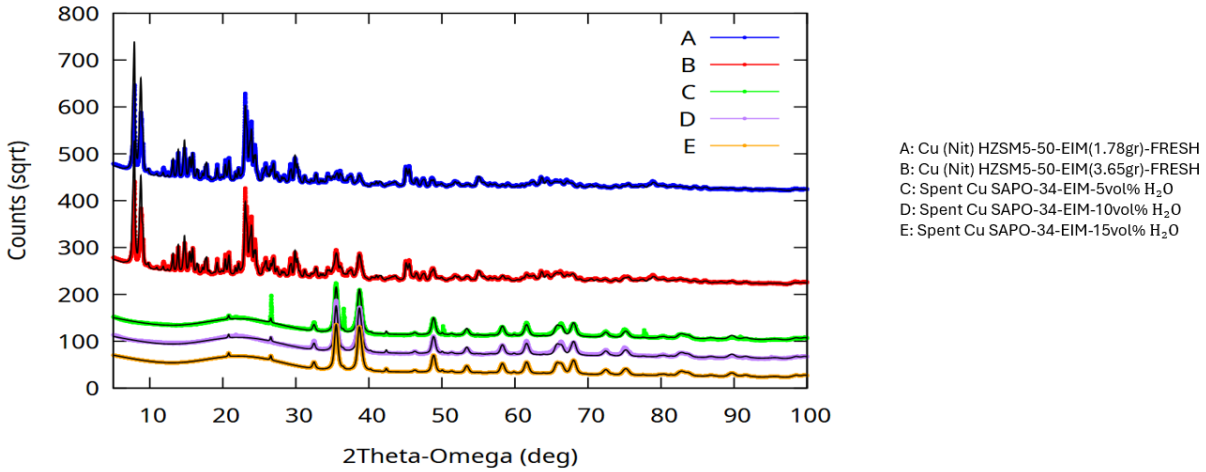

Figure 9.3: X-ray diffraction (XRD) patterns of fresh and spent Cu-containing catalysts: (A) fresh Cu(Nit)–HZSM-5 (1.78 g), (B) fresh Cu(Nit)–HZSM-5 (3.65 g), (C) fresh Cu SAPO-34-EIM, (D) spent Cu SAPO-34-EIM after reaction in the presence of 10 vol% H_2O, and (E) spent Cu SAPO-34-EIM after reaction in the presence of 15 vol% H_2O, illustrating the effect of hydrothermal reaction conditions on catalyst crystallinity and structural stability.

Figure (9.3) shows the X-ray diffraction (XRD) patterns of fresh and spent Cu-containing catalysts, including Cu(Nit)–HZSM-5 and Cu SAPO-34 after reaction under wet conditions with varying water concentrations (5–15 vol% H_2O). The fresh Cu(Nit)–HZSM-5 samples (A and B) display well-defined and intense diffraction peaks characteristic of the MFI framework, confirming their high crystallinity prior to reaction. In contrast, the fresh Cu SAPO-34 catalyst (pattern C) exhibits the characteristic reflections of the CHA-type SAPO-34 structure, indicating successful framework formation and good structural order before catalytic testing. After reaction at high temperature under wet conditions, the spent Cu SAPO-34 samples (patterns D and E) retain the main CHA diffraction peaks; however, a noticeable decrease in peak intensity and slight peak broadening are observed, particularly with increasing water concentration. This loss of crystallinity suggests partial hydrothermal degradation of the SAPO-34 framework during reaction, which becomes more pronounced at higher H_2O levels. No distinct diffraction peaks corresponding to bulk CuO or other crystalline copper phases are detected in the spent catalysts, indicating that copper species remain highly dispersed or present as amorphous phases below the detection limit of XRD. The observed structural degradation of the SAPO-34 framework under wet, high-temperature conditions correlates well with the rapid

deactivation and reduced catalytic activity seen in the time-on-stream experiments, confirming that hydrothermal instability plays a key role in limiting the performance of Cu SAPO-34.

9.2 Nominal loading:

Copper loading on zeolite supports via the EIM method using copper nitrate as the precursor, with Cu loadings of 1.78 g and 3.56 g.

$$\text{Cu metal weight \%} = \frac{63.54\ g\frac{Cu}{mol} \times 3.56\ g\ of\ copper\ (II)\ nitrate\ trihydrate}{241.60\ g(copper\ (II)\ nitrate\ trihydrate)/mol} = 0.93\ \text{g Cu}$$

$$\text{Cu weight \% on each 10g support} = \frac{0.93\ g\ metal}{10.93\ g\ catalyst} = 8.5\ wt\%$$

$$\text{Cu metal weight \%} = \frac{63.54\ g\frac{Cu}{mol} \times 1.78\ g\ of\ copper\ (II)\ nitrate\ trihydrate}{241.60\ g(copper\ (II)\ nitrate\ trihydrate)/mol} = 0.46\ \text{g Cu}$$

$$\text{Cu weight \% on each 10g support} = \frac{0.46\ g\ metal}{10.46\ g\ catalyst} = 4.39\ wt\%$$

9.3 Scanning electron micrographs of Cu modified ZSM-5 synthesized catalysts

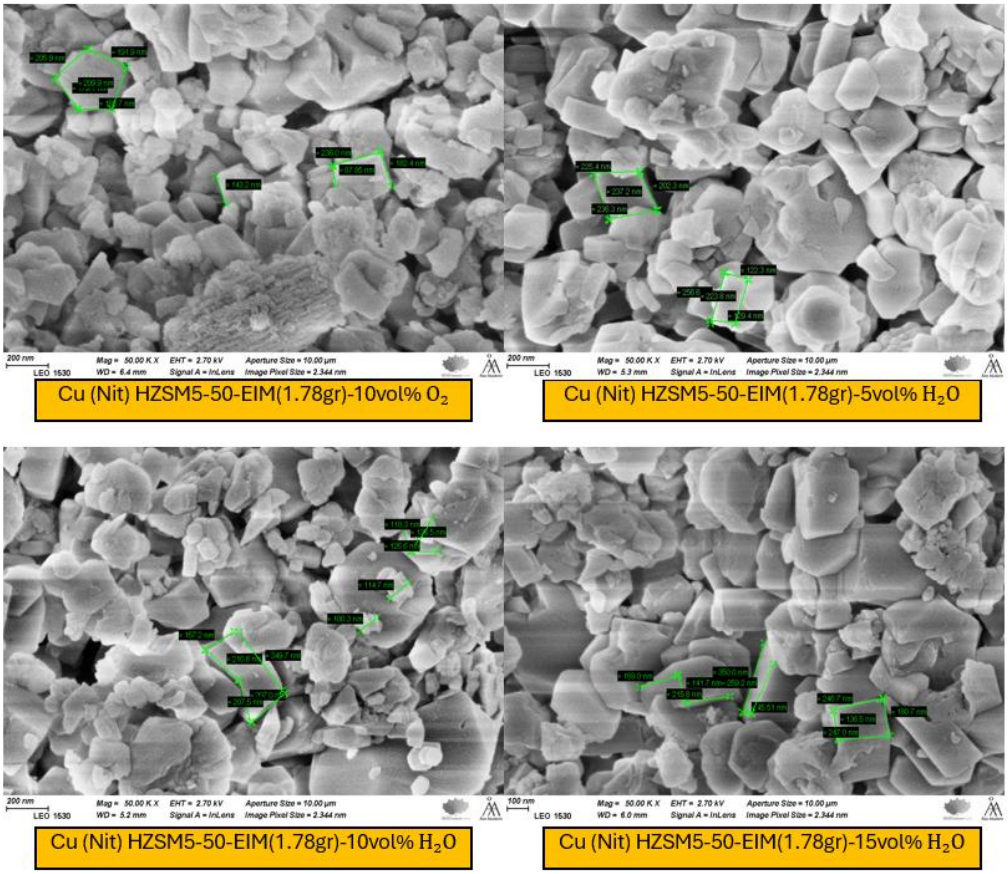

Figure 9.4: SEM images of spent Cu (Nitrate)–HZSM-5-EIM catalysts with 1.78 g Cu loading after reaction under different conditions: 10 vol% O_2, 5 vol% H_2O, 10 vol% H_2O, and 15 vol% H_2O. Green markers indicate representative crystal size measurements.

Scanning electron microscopy (SEM) was utilized to analyse the surface structure and particle size distribution of the Cu (Nitrate)–HZSM-5-EIM catalyst with a copper content of 1.78 g following exposure to various reaction settings, such as oxygen-rich and humid conditions. Figure 9.4 illustrates that all samples retain the typical coffin-shaped morphology of ZSM-5 crystals, signifying that the zeolite framework stays structurally stable post-reaction. At O_2 levels 10 vol%, the catalyst shows distinct crystallites primarily within the particle size range of about 180–300 nm, indicating minimal agglomeration and strong structural integrity. Upon exposure to 5 vol% H_2O, the crystal structure remains mostly intact; nonetheless, a minor rise in surface roughness occurs, with particle sizes measured between approximately 200 to 260 nm. Raising the water concentration to 10 vol% H_2O leads to stronger crystal–crystal interactions and localized agglomeration, with particle sizes generally varying between approximately 170 and 350 nm. At the maximum water concentration of 15 vol% H_2O, the catalyst exhibits the highest level of surface roughness and clumping, with particle sizes generally between 180–320 nm. No clear copper oxide particles are visible on the outer surfaces of the samples, suggesting that copper species are either highly dispersed or restricted within the zeolite pores. The slow rise in particle size and agglomeration with higher water content aligns with hydrothermal impacts and is linked to the diminished catalytic stability noted during time-on-stream studies

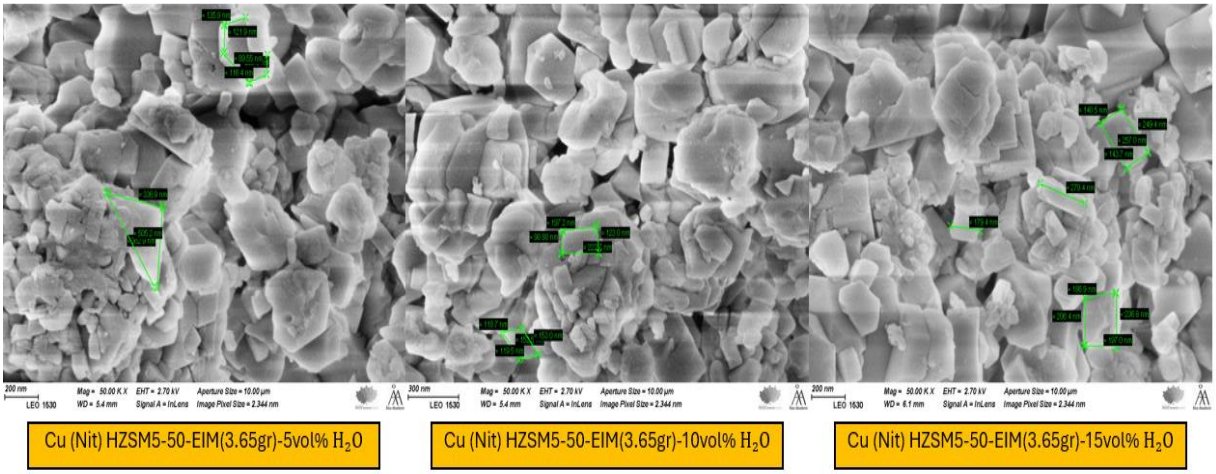

Figure 9.5: SEM images of spent Cu(Nitrate)–HZSM-5-EIM catalysts (Cu loading: 3.65 g) after reaction under wet conditions: 5 vol% H₂O, 10 vol% H₂O, and 15 vol% H₂O, showing the effect of water concentration on crystal morphology and surface features.

Scanning electron microscopy (SEM) was used to investigate the surface morphology and structural integrity of the Cu(Nitrate)–HZSM-5-EIM catalyst (3.65 g Cu loading) after exposure to wet reaction conditions with varying water concentrations (5, 10, and 15 vol% H_2O). As shown in Figure (9.5), the spent catalysts retain the characteristic coffin-shaped morphology of the ZSM-5 crystals, indicating that the overall zeolite framework remains structurally intact after reaction. At 5 vol% H_2O, the crystals appear well-defined with relatively smooth surfaces and limited agglomeration, suggesting minimal structural degradation. Increasing the water concentration to 10 vol% H_2O results in a slightly rougher surface texture and more pronounced crystal–crystal contacts, which may indicate the onset of hydrothermal effects and partial surface restructuring. At the highest water concentration of 15 vol% H_2O, more noticeable surface irregularities and local agglomeration are observed, although the primary ZSM-5 crystal morphology is still preserved. No distinct copper oxide particles are visible on the external surface in any of the samples, implying that copper species are either highly dispersed or located

within the zeolite pores. These observations suggest that increasing water concentration promotes gradual surface modification and agglomeration effects, which correlate with the reduced catalytic stability observed during time-on-stream experiments, while the ZSM-5 framework itself remains largely resistant to severe hydrothermal collapse.